MINISTRY OF TECHNOLOGY

AERONAUTICAL RESEARCH COUNCIL
REPORTS AND MEMORANDA

Experiments with Cones in Low-Density Flows at Mach Numbers near 2

by
E. W. E. ROGERS, C. J. BERRY and MISS B. M. DAVIS

Experiments with Cones in Low-Density Flows at Mach Numbers near 2

by

E. W. E. Rogers, C. J. Berry and Miss B. M. Davis

Summary.

Tests have been made on the N.P.L. low-density tunnel on two pressure-plotting cones of 15 deg and 30 deg semi-vertex angle placed at zero incidence to the flow. The stream static pressure was varied between 20 and 80 microns of mercury, giving Reynolds numbers, based on a model length of 1·25 inches and free-stream conditions, of from 81 to 372. The tunnel Mach number varied between 1·92 and 2·24 as the tunnel static pressure changed.

On the forward-facing surfaces the local pressures are higher than those for inviscid flow and it is shown that this viscous-interaction effect can be reasonably well predicted by a simple theory using a tangent-cone technique. The base pressures on both cones were measured and the results agree well with data obtained earlier by Kavenau[18]. The flow behind the model was explored in a simple manner and is shown to resemble that obtained on blunt-based bodies at higher Reynolds numbers.

The tips of both models were progressively blunted by means of truncations normal to the cone axes, and the changes in the surface pressure distributions were measured. For the cone with a 30 deg semi-vertex angle these changes were quite small.

Some details of the tunnel operating technique and the instrumentation (including the thermistor pressure-measuring system) are given in an Appendix.

CONTENTS

---

1. *Introduction.*

One of the most distinctive features of transition and continuum low-density flows is the presence of thick, rapidly-growing laminar boundary layers. At these low Reynolds numbers the streamlines in the inviscid flow away from the body surface are significantly distorted by the boundary-layer growth, an effect usually referred to as viscous interaction. The increase in surface pressure resulting from the viscous interaction is the viscous-induced pressure increment, and the magnitude of this is directly related to the boundary-layer growth.

Viscous-induced pressure changes are perhaps most noticeable when the boundary-layer develops along a flat surface; in two-dimensional flow the most obvious example is the flat plate, and in axisymmetric flow the cone. The changes are likely to be of greatest significance on slender bodies, where the streamline displacement effect caused by the solid boundary may no longer be large compared with that due to the boundary layer.

Some earlier workers were interested in the magnitude of the viscous-interaction effect on slender cones because of the possible use of these shapes as static probes in rarified supersonic air flows[1]. Later problems of viscous-induced pressures on a cone became of interest in itself, particularly after the appearance of a theoretical paper by Probstein[2] in 1955 dealing with laminar hypersonic flow over an unyawed cone. This showed that the induced pressures in this problem could be correlated through a viscous-interaction parameter χ, equal to $\sqrt{C} \, M^3 / \sqrt{Re}$, where C is the Chapman-Rubesin factor linking viscosity and temperature, M and Re are suitably-chosen Mach and Reynolds numbers in the flow. Experimental work by Talbot, Koga and Sherman[3] in 1958 demonstrated that this hypersonic approach was reasonably valid for slender cones at Mach numbers between 3·7 and 5·7, but that use of a tangent-cone and exact cone-flow tables to predict the magnitude of the interaction effect was rather better. Somewhat earlier Ipsen[4-6] had measured, with a force balance, the overall drag of the forward-facing surfaces of a cone of 15 deg semi-vertex angle at Mach numbers near 2 and 4, and showed that the measured force could be estimated reliably from a knowledge of the inviscid pressure drag, the pressure-drag increase associated with the viscous-induced pressure changes, and the surface-friction drag due to the boundary layer. The last component includes the contribution arising from the transverse curvature of the boundary layer as it develops along the cone surface (*see* Ref. 7).

Up to the present most of the work on low-density cone flows has been undertaken at high supersonic speeds using cones with small semi-vertex angles. It was felt therefore that data from cones with a fairly large semi-vertex angle and tested at a moderate supersonic Mach number might be of interest, particularly as the flow could not be regarded as hypersonic. The first experiment in the recently-commissioned N.P.L. low-density tunnel was designed with this aim in mind; at the same time the experiment allowed the necessary experimental techniques (pressure plotting, flow visualization and exploration, and tunnel operation) to be brought fully into use.

2

It was decided to measure the pressures on the surfaces of two cones with semi-vertex angles (θ_c) of 15 deg and 30 deg when placed at zero incidence in a nozzle giving a flow Mach number of about 2. These pressures and those at a point on the cone base were measured for stream static pressures between 20 and 80 microns of mercury[+], almost the full operating pressure range of the tunnel. As a subsidiary experiment the noses of the two cones were truncated in progressive stages and the surface and base pressures re-measured. Some simple pitot traverses were made in the wake of the model in an attempt to understand the nature of the wake flow.

The experiment occupied the tunnel at intervals between May and November, 1963.

2. Experimental Details.

2.1. The Tunnel.

The N.P.L. low-density tunnel, a photograph of which is included as Fig. 1a, was erected in 1961 and began to run in the following year. A considerable time was spent developing the required measuring and operating techniques, and in exploring the flow in the two contoured nozzles initially available. These, based on the data given in Refs. 8 and 9, were designed for nominal Mach numbers of 2 and 4 and are operated at atmospheric stagnation temperature. To obtain higher Mach numbers without liquefaction of test-section air an electric heater is available which can raise the stagnation temperature of the air upstream of the nozzle to about 830 deg K. This heater was not used in the present tests and the average stagnation temperature was close to 283 deg K, the value actually used in calculating the flow Reynolds numbers.

The tunnel flow is obtained by a pumping system using three types of pumps in series. Five oil-diffusion pumps[*] extract the air at low pressure from the large test chamber surrounding the nozzle exit (Fig. 1b and Fig. 2) and discharge it to five Roots-type rotary pumps[†]. These in turn discharge to two rotary piston pumps[†], from which the air is finally exhausted at a pressure just above the atmospheric value. The volume flow of the pumping system varies with the pressure in the test section (Fig. 3). Ideally this flow should be matched to that delivered by the nozzle (including the contributions from both the central isentropic core and the thick surrounding boundary layer).

The air entering the tunnel settling chamber upstream of the nozzle is dry, with a frost-point at about 220 deg K. The stagnation temperature (T_0) of the air is measured and its total pressure (H_0) controlled by a series of valves and measured on an accurate manometer. The volume flow of the air entering the tunnel is determined from a Rotameter. The pumping system draws air from the large test chamber surrounding the nozzle exit and this pressure (p_t) must be known accurately. The fundamental standard used for this is a McLeod gauge, with an Alphatron gauge and a thermistor manometer as secondary standards calibrated in terms of the McLeod gauge. Brief details of these instruments will be found in the Appendix.

The pressure of the nozzle at its exit must be carefully balanced with the pressure p_t in the test chamber, otherwise the jet experiences a distortion as it enters the chamber, and both axial and transverse pressure gradients are present in the neighbourhood of the model. The design for the nominal $M = 2$ nozzle used for the present tests, which has an exit diameter of 7·24 in., was based on an initial estimate of the pumping-system volume flow which was somewhat larger than that found later to be achieved at the upper end of the static pressure range; some degree of inbalance must therefore be accepted. The effects of this lack of balance could be reduced considerably if a transparent plastic extension (or 'skirt') of length 7 in. and with a slowly increasing cross-section was added to the nozzle exit (see Fig. 1b). This improvement was achieved at the expense of a thicker boundary layer at the new model position, near the skirt exit, and hence a smaller useful core of isentropic flow. The plastic skirt, with an 8·00 in. exit diameter, was used

[+] The mean free paths for these extremes of the test range are 0·043 in. and 0·010 in respectively.
[*] Edwards Model 30B4.
[†] Edwards Model 1R5.
[†] Edwards Model 1SC3000.

for the cone tests and the nozzle-flow pressure (p_w) measured at a hole on the wall of the skirt 1·9 in. upstream from the skirt exit. Balance was attempted between this pressure and that in the test chamber. The success that can be achieved is illustrated in Fig. 4; unbalanced conditions are seen to exist for values of p_w above 50μ, where μ is one micron of mercury pressure*. The effect of the lack of balance on the tunnel flow and on the experimental results will be discussed later.

For flow exploration, the tunnel is equipped with a three-way traverse gear (see Fig. 1b), operated remotely from outside the tunnel and capable of exploring any part of the nozzle and test section. Up to the present only pitot probes have been used since the characteristics of these in supersonic, low-density flow are now fairly well defined. The flow density in the working region of the tunnel, though higher than that of the almost stationary air in the chamber, is too low to enable conventional schlieren or shadowgraph flow visualization methods to be used; instead an afterglow visualization system is available, very similar to the design developed by workers at the University of California (Berkeley)[10]. Two different techniques may be employed, one using pure argon, the other air enriched with nitric oxide, as the test gas. At the N.P.L. the former method has been most successful and results presented as Fig. 27 in the present report were obtained with argon afterglow. The brightest glows are obtained when the tunnel static pressure is about 25μ; at higher stream pream pressures, ionization of the argon in the high-pressure region upstream of the nozzle becomes progressively more difficult.

The tunnel is also fitted with a force balance for the direct measurement of overall forces on models mounted in the stream. This balance was not used during the cone tests, which were principally concerned with the measurement of pressures on the forward-facing surfaces of the models and on their bases. Such measurements require manometers of the highest possible accuracy over a range between 3μ and 300μ. Early experience at the N.P.L. had suggested that a simple U-tube, filled with a low vapour-pressure oil and observed from outside the test chamber by means of a low-powered travelling microscope did not give sufficient accuracy over the lower part of the pressure range. A thermistor manometer was therefore developed and a bank of these employed to measure simultaneously the model pressures and the tunnel pressures p_t and p_w. Frequent calibration of the thermistor manometer against primary or secondary standards is required in order to monitor the slow zero drift; in practice this does not prove arduous. A full description of the thermistor pressure-measuring technique is given in Section A.2 of the Appendix.

2.2. Tunnel Calibration and Performance.

Before the start of the present tests the nozzle flow had been traversed in both the axial and cross-stream directions with a calibration pitot tube and the local Mach number deduced from the pitot pressure (H'_1) and the total pressure in the settling chamber (H_0). In high Reynolds number supersonic flow a correctly-aligned pitot tube should measure the ideal pitot pressure (H_1) and the Mach number can then be obtained directly from normal-shock tables in terms of the ratio H_1/H_0. At low Reynolds numbers, however, the pitot pressure is not necessarily equal to its ideal value and prior calibration is required to determine the ratio H'_1/H_1 as a function of some flow parameter, frequently the Reynolds number formed from the pitot external diameter and the free-stream conditions (Re_d).

The present N.P.L. calibration probe is of $\frac{3}{8}$ in. external diameter, with a sharp-edged orifice and a 10 deg external chamfer. The wall thickness of the tube is $\frac{1}{32}$ in., giving an internal diameter of $\frac{5}{16}$ in. At the lowest stream static pressure (20μ) and a Mach number of 1·95, Re_d has a value of about 25. Tests by Enkenhus[11] on similar externally-chamfered probes at low supersonic Mach numbers show that the ratio H'_1/H_1 is about 1·01 at this condition* and decreases to just below unity for higher values of Re_d. Similar results were obtained by Sherman[12] for sharp-edged pitot tubes with an internal chamfer. The viscous correction to the calibration probe is therefore comparatively small over the complete range of the tunnel.

---

*A second, smaller $M = 2$ nozzle is being made to allow balanced conditions to be achieved in this upper part of the operating range.

*This ratio can become quite large; at $Re_d = 7$ it is nearly 1·4, according to Enkenhus' tests.

Typical distributions of Mach number along the skirt axis are given in Fig. 5a at static-pressure levels of 30, 50 and 67 μ. At the lowest pressure the distribution of Mach number is almost constant along the skirt and into the test chamber indicating, since the jet is balanced ($p_w = p_t$), that the increase in skirt diameter in the downstream direction is just sufficient to balance the growth in boundary-layer displacement thickness. At $p_w = 50\mu$, the boundary layer grows less rapidly and in the region $-2\cdot5$ in. $< x <$ $< -1\cdot0$ in., the stream Mach number (M_0) rises. This increase is offset near the exit plane by the 1μ difference between p_w and p_t, the axial variation in M_0 becoming very small. Finally at the highest pressure in this Figure ($p_w = 67\mu$) there is a longitudinal Mach number gradient extending well into the nozzle and induced as a direct result of the lack of balance between p_w and p_t. Presumably the excess pressure in the chamber penetrates upstream through the very thick boundary layer on the skirt wall, causes this to thicken and so compress the flow upstream of the skirt exit plane.

In all cases the cross-stream distribution of Mach number was reasonably uniform over the central isentropic core of the flow which represents the test region (Fig. 5b). Because of increased boundary-layer growth this core decreases in size as the stream static pressure falls, as shown in Fig. 5c. The edge of the core has been arbitrarily defined as the position at which the loss of pitot pressure in the nozzle boundary layer exceeds $0\cdot005\ H_0$. The core becomes very small at the lower test pressures, reducing to a diameter of about $0\cdot5$ in. at $p_w = 20\mu$. The base diameter of the large model is nearly $1\cdot44$ in. so that some difficulty in interpreting the data might be anticipated for this model at low pressures; as will be seen later certain effects attributable to this effect were observed. At $p_w = 30\mu$, only a small degree of interference should exist at hole 6 on the larger model. The core size also decreases slightly for stream pressures above 60μ; the nozzle boundary layer at the exit plane has an increased thickness because of the out-of-balance pressure difference between the nozzle flow and the test chamber.

Except for some flow-visualization work, all tests were made with the cones (of length $1\cdot25$ in.) mounted in the position shown in Fig. 5a, with the tip $0\cdot75$ in. inside the skirt and the base $0\cdot50$ in. downstream of the skirt exit plane. It is clear that for stream pressures above about 60μ there will be a pressure gradient along the length of the model, with the highest pressures towards the rear. At $p_w = 20\mu$ there is a similar, smaller pressure gradient associated not with the out-of-balance condition but with the large growth of the nozzle boundary layer at this low pressure.

For the present tests it was decided to use a stream Mach number (M_0) at the mid-point of the model and to correct measured flow quantities for the longitudinal pressure gradient when this was possible and desirable. The variation of this mean flow Mach number with p_w is shown in Fig. 6. Two sets of results are from early calibrations (including those contained in Fig. 5a) and additional points were obtained during the progress of the cone tests. The extent of the Mach number variation over the model position is shown. The stream Mach number rises as the pressure increases from 20μ to 50μ because of the reduced boundary-layer growth rate. Above $p_w = 50\mu$, M_0 falls as the out-of-balance condition becomes important. In the absence of this effect the stream Mach number would rise steadily with p_w (*see* Ref. 8, for example). There is some scatter in the results shown in Fig. 6, and in part this may be due to small day-to-day variations in the performance of the tunnel pumping system.

Whilst the test flow may be balanced in the empty-tunnel condition (or with no apparent change in observed pressures when the calibration pitot is in place) it is not obvious that this balance, and the calibration Mach numbers, are achieved when the models are in position. It is possible, for example, for the increased blockage associated with the flow field about and behind the cones to influence the boundary-layer growth upstream of the model position, and hence the Mach number just ahead of the model. This would be analogous to the out-of-balance interference discussed earlier.

To investigate this point two dummy models were made, of similar size to the test cones, but with $\frac{1}{8}$ in. diameter pitot tubes projecting for $\frac{1}{4}$ in. ahead of the cone tip. The pitot-cone combinations were mounted at the test position and the probe pressures read for flow conditions corresponding to changes in p_w of from 20μ to 80μ. In addition a similar pitot tube was tested on its own and its readings compared with those obtained for the two dummy cone models. The ratio of measured pitot pressure to stream total pressure (H'_1/H_0) for these three pitot models is shown in Fig. 7. The results for the small pitot alone and when in combination with the 15 deg cone are almost identical, indicating that the Mach number at the cone apex is not influenced by the cone flow field. A small effect can be detected with the larger cone

and this is most significant at the lower stream pressures. The usable core is then smallest (accentuating blockage effects), and the Mach number approaches that for detachment on a 30 deg pointed cone. These tests seem to indicate that the mean calibration line drawn in Fig. 6 is reasonable under most conditions, but that a small adjustment should be made for the larger cone at $p_w = 20\mu$; the stream Mach number at this pressure was therefore reduced from 1·95 to 1·92 for this model.

Fig. 7 also contains the curve of H'_1/H_0 for the $\frac{3}{8}$ in. diameter calibration probe, for which H'_1 is very close to H_1 over the test range. The difference between the full and broken lines in this Figure must be due to the viscous effect present for the smaller tube; hence the approximate correction factor H'_1/H_1 for this tube may readily be found. For the $\frac{1}{8}$ in. diameter probe this quantity is plotted against Re_d in Fig. 8(a). There is a marked increase in the factor as Re_d falls but the curve might be expected to lie closer to those obtained for chamfered probes by Enkenhus[11] and Sherman[12]. An explanation for this discrepancy is best sought by noting that for the N.P.L. probe the ratio of external to internal diameter (d/d_i) is 2·0, whereas Enkenhus used probes with much thinner walls. In the case d/d_i was usually less than 1·26. If it is accepted that the Reynolds number of the orifice (i.e. Re_{d_i}) is a more relevant parameter than Re_d, then the N.P.L. results can be rescaled so that Re_d is based on a fictitious thin-walled tube with d_i equal (as before) to $\frac{1}{16}$ in., but with d now equal to 1·25 d_i. The new curve is in much closer agreement with the Enkenhus and Sherman data. Indeed the significance of basing the probe Reynolds number on the orifice diameter and not the external diameter is best illustrated in Fig. 8b, where Enkenhus' results have been recast in this form and where they can be compared with the N.P.L. data. The agreement is good.*

The foregoing argument serves to provide a rough calibration for the small $\frac{1}{8}$ in. diameter pitot, sufficient to obtain approximate Mach numbers in the cone flow field; this aspect will be discussed later.

2.3. The Models.

Two basic models were used for the tests described in this report. Both were brass cones with an overall length (L) of 1·25 in., but with 15 deg and 30 deg semi-vertex angles respectively. Along a single generator of each cone were six pressure holes of 0·010 in. diameter, at the following positions (see also Fig. 9):

Hole No.	1	2	3	4	5	6
x/L	0·14	0·28	0·44	0·60	0·76	0·92

There was a further hole on the base of the model two-thirds of the base radius from the axis. Both models were supported entirely by their pressure tubes which gave an effective sting diameter of 0·15 in., the cross-stream support being placed 4 in. from the cone base to minimize support interference. P.V.C. tubing of 1 mm bore, and 12 in. long was used to connect the ends of the pressure tubes from behind the cross-stream support to the thermistor manometer bank, placed just outside the issuing jet.

After the initial tests were complete, both cones were progressively truncated in four stages, called for convenience States B to E. State A is the initial sharp-pointed condition.** The truncation was made very simply by cutting off the cone tip in a plane normal to its axis. In terms of x/L measured on the pointed model the new tip position was as follows:

State	A	B	C	D	E
x/L of tip	0	0·08	0·12	0·16	0·20

These truncations are illustrated in Fig. 9.

---

*The evaluation of the large ($\frac{3}{8}$ in. diameter) calibration probe is not affected by this argument, as its ratio of internal to external diameter was close to those values used by Sherman and Enkenhus.

**The diameter of the 'tip' on the sharp-pointed model was about 0·005 in.

At a later stage in the tests two other sharp-pointed pressure-plotting cones with $\theta_c = 15$ deg and 30 deg were used in conjunction with cylindrical afterbodies extending downstream from the base for one cone length L.

2.4. Experimental Procedure.

The cone surface pressures in all states were measured with the cones at zero geometric incidence and at values of p_w of 20μ to 80μ, in intervals of 10μ.

The pumping system is supplied with dry air from two sources, the main flow passing through the nozzle, and a secondary flow through the bypass pipe (see Fig. 2). Both supply lines are controlled by needle valves and the nozzle mass flow is determined by means of a flowmeter and an accurate pressure gauge.

For the present tests the sensitivity of the various thermistor manometers was chosen to be about 2μ/mm galvanometer deflection for the model surface pressures, 1μ/mm for the model base pressure and $\frac{3}{4}\mu$/mm for p_w (and other nozzle wall pressures). The required zero settings were determined by a preliminary tunnel run at the lowest value of p_w; following this a static calibration was made (i.e. with no flow through the nozzle) against the reading of the tunnel McLeod gauge for pressures up to 80μ, the tank pressure being directly controlled by the bypass flow. Above this pressure the pumping characteristics did not permit control over a wide pressure range, so the pumps were isolated from the test chamber, whose pressure was raised as required by admitting air through the control valve. The leak rate of the chamber is so small that no noticeable increase occurs during the time necessary to read the McLeod gauge. With the full static calibration completed, the tunnel was run at increasing values of p_w and pressure measurements obtained until the limit of the range of one of the thermistor manomenters was reached; the calibration was then checked. The zeros were reset and the whole procedure repeated for higher pressures, until the full range of p_w (20μ to 80μ) had been covered. At each pressure the greatest possible care was taken to ensure that p_w and p_t were in balance, or if this was not possible, that the difference in pressure was a minimum. Surface pressure readings for the seven values of p_w could be obtained in one day.

3. Results.

3.1. Cone Surface Pressures.

Because the present tests were intended to provide information on the departures from inviscid supersonic cone flow caused by the thick laminar boundary layer, it is convenient to plot the measured pressures (p) in terms of $(p - p_{ic})/p_{ic}$, where p_{ic} is the surface pressure given by the exact cone-flow solution in inviscid flow[13] at the same stream Mach number as the experimental results. This ratio is thus a direct measure of the viscous-interaction effect. The stream static pressure is best considered in terms of a Reynolds number (Re_L), based on the length L and free-stream conditions. Fig. 10 (derived from data in Ref. 8) shows how the Reynolds number per inch per micron static pressure varies with Mach number, assuming isentropic flow through the nozzle.

The pressure distributions for the 15 deg cone at six different model Reynolds numbers (and slightly different Mach numbers) are plotted together in Fig. 11. These results are plotted separately in Fig. 12. Similar information for $\theta_c = 30$ deg is contained in Figs. 13 and 14, together with data for $p_w = 80\mu$; results obtained at this pressure on the 15 deg cone later proved to be unsatisfactory.

As the test Reynolds number increases, there is a progressive change in the shape of the induced-pressure distribution along the cone surface. This is best illustrated in Fig. 13. The induced pressure is highest near the apex and is there most influenced by the stream Reynolds number. Further to the rear the Reynolds number effect is small and is masked by a marked fall in pressure below the inviscid cone value at the most rearward pressure hole. This is due to an upstream influence (through the thick boundary layer) of the low-pressure zone on the base of the cone. At $Re_L = 81$ ($p_w = 20\mu$) and $\theta_c = 30$ deg, the rear two holes are appreciably outside the usable core of the flow and therefore depart significantly from the general trend. The progression with Re_L is less ordered for $\theta_c = 15$ deg (Fig. 11), and there is some anomaly in the overall level of the data at $Re_L = 322$. The general pattern, however, resembles that exhibited by the larger cone, though the pressure increment at hole 5 is substantially higher for $\theta_c = 15$ deg. The fall in pressure at hole 6 is again evident.

7

A simple, theoretical estimate may be made of the induced-pressure effect on the two cones by using a tangent-cone approach similar to that outlined in Appendix A of Ref. 3. The boundary layer is assumed to grow along the cone surface in some prescribed manner so that the rate of change of displacement thickness $(d\delta_c^*/ds)$, (where s is measured along the surface from the vertex) may be regarded as an effective change in the cone angle from θ_c to $\theta_c + \theta_\delta$, with

$$\theta_\delta = \tan^{-1} \left(\frac{d\delta_c^*}{ds} \right).$$

The pressure at any point on the cone surface is then assumed to be that on a cone of semi-vertex angle $\theta_c + \theta_\delta$. The boundary-layer displacement thickness at position s on a flat plate with adiabatic wall conditions, Prandtl number of 0·725, specific-heat ratio 1·40, and Chapman-Rubesin factor C equal to unity may be written[14] as

$$\frac{\delta^*}{s} = \frac{1·730}{\sqrt{Re_s}} [1 + 0·26\, M_s^2]$$

where the suffix s refers to flow conditions just outside the surface boundary layer. For a cone the Mangler transformation[15] may be used; the displacement thickness is then $1/\sqrt{3}$ times the corresponding thickness on a flat plate. Hence to good approximation

$$\frac{\delta_c^*}{s} = \frac{1}{\sqrt{Re_s}} [1 + 0·26\, M_s^2] \tag{1}$$

and

$$\frac{d\delta_c^*}{ds} = \frac{1}{2\sqrt{Re_s}} [1 + 0·26\, M_s^2] = \tan \theta_\delta \tag{2}$$

assuming that M_s does not change with s. As a first approximation M_s may be assumed to have the value for inviscid flow over a cone of half-angle θ_c at the test Mach number, and Re_s can be based on flow conditions to the rear of the associated shock. Once θ_δ has been found along the cone surface and added to θ_c, the variation in surface pressure may easily be found from suitable cone tables or graphs. It is then necessary to recalculate θ_δ using the new cone-surface conditions in the estimation of Re_s and M_s, and to evaluate again the surface pressure. This iteration procedure will continue until reasonable convergence has been achieved; in practice it was found that negligible change resulted if the sequence was taken beyond the third approximation. Typical changes in $(p - p_{ic})/p_{ic}$ which accompany the successive approximations are illustrated in Fig. 15, and there compared with the experimental data. A marked reduction in the induced-pressure parameter occurs at the second approximation; further calculation, however, leads to significant changes only over the front part of the model.

The results of this approximate tangent-cone (TC) calculation are compared with experiment in Figs. 12 and 14. Considering the simplicity of the approach, the agreement obtained is good. The most noticeable discrepancy occurs at $Re_L = 81$ for $\theta_c = 30$ deg (Fig. 14a), but, as was mentioned earlier, the rear part of the model lies inside the tunnel boundary layer for this condition. It is possible that this effect (which is most serious for holes 5 and 6) also influences the pressure further upstream on the model surface.* In general, the TC theory seems to overestimate slightly the actual surface pressures; a similar trend is apparent in Ref. 3 for slender cones at higher Mach numbers.

---

*Some interference might be expected from the reflection of the bow wave from the boundary layer when the core is small. Flow visualization shows, however, that the 'reflection' takes place from a point well inside the boundary layer, and it therefore seems that this form of interference is less important.

The theoretical method outlined above can of course be criticized on a number of points. The simple displacement-thickness equation (1), though reasonably valid for high-Reynolds-number continuum flow with zero pressure gradient, is less certain under the present conditions. The validity of the Mangler transformation must also be questioned when it is applied to thick boundary layers. Probstein and Elliott[7] show that it may be used, providing the value of δ_c^*/r_s (where r_s is the body radius at the station s) is not too large. The ratio δ_c^*/r_s is a measure of the transverse curvature imposed on the developing boundary layer and to the first approximation the displacement thickness is unaltered by this transverse curvature provided δ_c^*/r_s is of order unity[2,7]. For the present tests δ_c^*/r_s is largest for the 15 deg cone and varies between 1·9 (for hole 1 at a stream pressure of 20μ) and 0·3 (for hole 6 at 80μ). The corresponding values for the 30 deg cone are about 40 per cent of these for the smaller cone.

Since δ_c^* is about the same order as r_s it would seem that the effects of traverse curvature on the viscous-induced may be ignored for the present tests, and it is perhaps sufficient only to note that the main effect of the transverse curvature would be to thin slightly the boundary layer and hence to reduce the predicted value of the induced-pressure parameter $(p - p_{ic})/p_{ic}$. The agreement between experiment and a theory which neglects transverse curvature effects may of course be used as evidence that such neglect is justified, and this view is reinforced by the results shown in Ref. 3, where good agreement was obtained between a tangent-cone theory (neglecting surface curvature) and experiment for $1 < \delta_c^*/r_s < 3$ at rather higher supersonic Mach numbers. It would seem in fact that the most significant effect of the transverse curvature is on the local surface friction and heat-transfer rates[2,6,7]; fortunately these quantities are not of direct interest in the present investigation.

Another possible source of error stems from the use of a tangent-cone method to predict the pressure on what is effectively an ogival-shaped body. The accuracy of the tangent-cone approximation is discussed in Ref. 16. In general the tangent-cone method gives surface pressures which are slightly too high, the deviation increasing with distance from the body vertex[3]. The errors are likely to be only a few percent, however, and may be neglected in the present context. The *TC* calculation also ignores the pressure gradient which may exist across the thick laminar layer, and moreover does not allow for the distortion of the boundary-layer profile due to the external pressure gradient. The iteration procedure, though taking account of simple changes in local Mach number and surface pressure, is not in itself without some source of error.

Probably some of these errors cancel, and some may well be very small. Lacking more detailed work on their individual influences it still seems reasonable to conclude that a simple, tangent-cone approach provides an effective method of estimating the induced-pressure increments on cones at moderate supersonic speeds.

The tangent-cone method may be simplified further (with some attendant loss in accuracy) to allow a comparison of the results obtained on a given cone in terms of the local Reynolds number. Following Probstein one may write

$$p = p_{ic} + \left(\frac{\partial p_{ic}}{\partial \theta}\right)_{\theta = \theta_c} \theta_\delta + \frac{1}{2}\left(\frac{\partial^2 p_{ic}}{\partial \theta^2}\right)_{\theta = \theta_c} (\theta_\delta)^2 + \ldots .$$

In terms of the parameter used in the present report

$$\frac{p - p_{ic}}{p_{ic}} = \frac{H_0}{p_{ic}} \left[\left(\frac{\partial(p_{ic}/H_0)}{\partial \theta}\right)_{\theta = \theta_c} \theta_\delta + \frac{1}{2}\left(\frac{\partial^2(p_{ic}/H_0)}{\partial \theta^2}\right)_{\theta = \theta_c} (\theta_\delta)^2 + \ldots \right] . \tag{3}$$

To obtain the derivatives of cone pressure with respect to θ,

let

$$\frac{p_{ic}}{H} = A\theta_c^2 + B\theta_c + K.$$

9

Then
$$\left(\frac{\partial(p_{ic}/H_0)}{\partial\theta}\right)_{\theta=\theta_c} = 2A\theta_c + B$$

$$\left(\frac{\partial^2(p_{ic}/H_0)}{\partial\theta^2}\right)_{\theta=\theta_c} = 2A.$$

The constants A, B and K can be found by fitting this curve through the exact values of p_{ic}/H_0 at cone angles of 15 deg, 30 deg and some intermediate value. The most important effect of Mach number is to change K, which does not affect the two derivatives. For the present flow conditions, it was found that $A = 0.667$, and $B = 0.0584$, if θ is measured in radians.

$$\left(\frac{\partial(p_{ic}/H_0)}{\partial\theta}\right)_{\theta=\theta_c} = \begin{cases} 0.407 & (\theta_c = 15°) \\ 0.756 & (\theta_c = 30°). \end{cases}$$

For both cone angles

$$\left(\frac{\partial^2(p_{ic}/H_0)}{\partial\theta^2}\right) = 1.334.$$

The boundary-layer equation (2) may be simplified by putting $\tan\theta_\delta = \theta_\delta$ and letting M_s have a constant value based on inviscid cone flow for some mean stream Mach number, say 2·10. Then

$$\theta_\delta = \frac{D}{\sqrt{Re_s}}\ \text{radians}$$

where D is 0·92 for $\theta_c = 15$ deg, and 0·73 for $\theta_c = 30$ deg. Evaluating H_0/p_{ic} also for $M_0 = 2·10$, one obtains for $\theta_c = 15$ deg

$$\frac{p-p_{ic}}{p_{ic}} = \frac{2·14}{\sqrt{Re_s}} + \frac{3·21}{Re_s} + \ \cdots \ , \tag{4a}$$

and for $\theta_c = 30$ deg

$$\frac{p-p_{ic}}{p_{ic}} = \frac{1·43}{\sqrt{Re_s}} + \frac{0·92}{Re_s} + \ \cdots \ . \tag{4b}$$

These equations are compared with the experimental data in Figs. 16a and b respectively; only the first four holes on each cone have been used* in order to avoid effects associated with the base flow. Though there is a certain amount of scatter, the agreement between theory and experiment is quite good. At $\theta_c = 30$ deg, the data appear to reproduce the non-linear trend predicted by using both terms of equation (4b), though this may be fortuitous. Indeed some alteration in the precision of the agreement can be obtained by varying the mean Mach number chosen for the theory (2·10), and because the stream Mach number varies with tunnel pressure, too much should not be made of the comparison between the theoretical lines and the experimental results. The main purpose of Figs. 16a and b is to demonstrate the dominance of the local Reynolds number in determining the magnitude of the induced-pressure effect.

---

*Three in the case of the 30 deg cone at $p_w = 20\mu$, because of possible interference of the small core diameter on the reading of hole 4.

For hypersonic flow the equivalent equation to (4) above may be written[2]

$$\frac{p - p_{ic}}{p_{ic}} = A'\chi_s + B'\chi_s^2$$

where χ_s is a hypersonic interaction parameter equal to $M_s^3/\sqrt{Re_s}$ (the Chapman-Rubesin factor is taken as unity) and A' and B' are constants. In deriving this the assumption is made, amongst others, that in the boundary-layer gradient equation (2), $0.26\,M_s^2$ is large compared with unity, which may therefore be neglected. This is certainly not so for the present tests, where $0.26\,M_s^2$ is of the order of unity.

3.2. Upstream Influence of Base Flow.

It was remarked earlier, and indeed is evident in Figs. 11 and 13, that the flow departs from that expected on an infinite cone over the last third or so of the model length. The surface flow is strongly influenced by the expansion of the boundary layer over the rear shoulder of the cone into the wake. Because the boundary layers are very thick at these low Reynolds numbers the upstream effect is particularly marked. If the influence is assumed (for convenience) to start at $x/L = 0.7$, the region affected amounts to a few boundary-layer thickness only, in strong contrast to the upstream influence observed during experiments on shock-wave and boundary-layer interaction on flat plates at moderate and high Reynolds number. In such cases the upstream effect is usually measured in tens of boundary-layer thicknesses. Similarly tests reported in Ref. 17 indicate that at a Reynolds number of about 10^6, the upstream influence of an expansion at the shoulder of a double-wedge wing was not less than twenty boundary-layer thicknesses. The comparatively small upstream influence is perhaps a little unexpected therefore, but is confirmed by Ref. 1 where a similar small effect was reported during experiments at $M_0 \simeq 4$ on a slender cone.

The influence of test Reynolds numbers on the upstream effect is not easy to determine from the existing data but the pressure fall between holes 5 and 6 certainly decreases as the tunnel pressure increases. This may be the result of a small increase in the base pressure with Reynolds number (see Section 3.3).

To investigate the base influence a little further, the cone surface pressure distributions were remeasured* when a cylindrical afterbody, of length L, was added to the cone. It was expected that this would alter the flow pattern behind the base and as a result modify the expansion at the rear of the cone. Rather surprisingly the pressures at hole 6 were very little altered by the presence of the afterbody; no significant changes could be detected at the other pressure holes. In Fig. 17 the two sets of pressure data for hole 6 are compared. The scatter is higher when the afterbody was fitted but the overall trend with Re_L is very similar to that obtained in the original tests.

It was felt that the results of Fig. 17 might be explained if it was assumed that the cylindrical afterbody was immersed in a large wake cavity, as in Fig. 18a. The presence of the afterbody does not then alter greatly the direction of the shear layer after it leaves the cone surface and only a limited flow expansion occurs at this position. An alternative flow for the cone alone is sketched in Fig. 18b; a strong expansion is associated with the shoulder flow and the base cavity is smaller. It is this type of flow which would be expected with isolated cones at higher Reynolds numbers. To pursue this a little further, traverses were made with a $\frac{1}{8}$ in. diameter pitot tube (similar to P_1 in Fig. 7) at three stations behind the 15 deg cone. The traverses were along lines normal to the tunnel axis, starting from well inside the nozzle boundary layer and ending inside the model wake. From this information it is possible to draw contours of constant pitot pressure (H'_1), and two examples of the resulting flow field are shown in Figs. 19a and b. The approximate relationship between H'_1 and local Mach number can be deduced from the pitot calibration curve (Fig. 8), if the total-pressure loss through the bow shock wave is neglected. In Fig. 19a the nozzle boundary layer is clearly shown, and this appears to end about 1·6 in. from the tunnel axis where H'_1 is around 500μ. The viscous wake is also well defined, as a region of rapid changes in H'_1; the outer edge corresponds approximately to the 450μ contour. The bow shock-wave position deduced from the traverses agrees

---

*A second pair of pressure-plotting models were used in these tests, which were made after those in which the original models were truncated.

well with a simple conical shock for a cone where $\theta_c + \theta_\delta = 20$ deg. This shock 'reflects' from the thick nozzle boundary layer as an expansion. Another expansion region, centred more or less on the outer edge of the boundary layer at the cone base is also evident. A further feature is the shape of the pressure contours for $H'_1 \leqslant 200\mu$ in the model wake. Though these are not streamlines of the flow, they do suggest a wake structure similar to that shown in Fig. 18b, and this impression is reinforced by the existence of the centred expansion region at he model railing edge.

Fig. 19b shows a similar diagram at a much lower static pressure; the flow pattern is less clear-cut, partly perhaps because of the interaction of the bow wave with the edge of the nozzle boundary layer almost at the cone trailing edge. A check on the shock position could be made at this pressure because argon afterglow visualization photographs were available for $p_w \simeq 25\mu$; for comparatively small disturbances to the free-stream (i.e. slender cones) the bow-shock angle in a monatomic gas is only slightly greater than for air. The contraction of the inner part of the wake flow, commented upon in connection with Fig. 19a, is again evident.

The approximate Mach number variation along the lines AA' in Figs. 19a and b is shown in Fig. 20a. The bow-wave compression, and the base-shoulder expansion can be clearly seen. At $p_w = 80\mu$ the 'reflected' expansion zone shows up, but this is not so obvious at the lower pressure. The base-shoulder expansion could in fact be seen visually (but not photographed*) in argon afterglow visualization tests, and moreover it was possible to detect the compression system associated with the re-expansion of the wake (see Fig. 18b). The compression appeared to originate about $1\cdot5L$ downstream of the base.

The foregoing evidence strongly suggests that for the isolated cone, the wake resembles that sketched in Fig. 18b rather than the large-cavity flow of Fig. 18a. The insensitivity of the pressure at hole 6 must be explained in other terms and the following explanation[†] is tentatively suggested.

The boundary layer approaches the cone shoulder (point C in Fig. 20b) and begins to be influenced by the corner flow at some upstream point J. A free interaction occurs between the subsequent boundary-layer development and the external pressure field arising from the deflection of the flow streamlines outside the boundary layer. At equilibrium the displacement thickness decreases steadily as the corner is approached and the rate of decrease must be precisely that which is compatible with the falling pressure associated with the progressive deflection of the external streamlines. The scale (i.e. shape and magnitude of the pressure distribution) of the interaction is determined solely by the local pressure, Mach number and boundary-layer characteristics at J. A similar interaction takes place downstream of the corner, this time with the separated shear layer, and the total adjustment of pressure is therefore shared in some way upstream and downstream of the corner. As the angle (α) of the flow deflection is increased, a greater expansion is demanded; p_c will decrease in consequence, but providing the boundary layer upstream of the interaction is unaltered, the pressure change will be affected by a lateral displacement of the original pressure distribution ($\alpha = \alpha_1$), without change of shape, until the new value of p_c (p_{c_2}) for $\alpha = \alpha_2$ is attained. Because the pressure gradients close to the corner are large but decrease rapidly away from this position the lateral adjustment in J for the new conditions is effectively very small. It follows also that a point like hole 6 lying within the interaction, but not too near the corner, will experience only a very small change in pressure as α is altered (see Fig. 20b).

In the present context α changes from that occurring in the flow sketched in Fig. 18b, to that where the flow is made to flow once again in the stream direction by the addition of the cylindrical afterbody ($\alpha = \theta_c$). Most of the required pressure change takes place in the immediate vicinity of the corner, leaving only a small alteration upstream at hole 6.

3.3. Base Pressures.

The ratio of the measured base pressure to the wall reference pressure (p_b/p_w) is plotted in Figs. 21a and b for both sharp-pointed cones (State A). There is a tendency for this ratio to increase with Re_L but at the higher static pressures, some of this increase is probably associated with the out-of-balance test-chamber

---

*Because a typical exposure time is 30 seconds, and because there are slight fluctuations in the flow pattern within that period, the fine structure visible to the eye does not appear in a photograph.

[†] Due to Mr. J. Nash of Aerodynamics Division, N.P.L.

12

pressure, which is higher than p_w. It seems reasonable to suppose that the base pressure would be strongly influenced by the pressure level outside the wake which is different from p_w in out-of-balance conditions. At the lowest test value of Re_L, the measured pressures were very low (between 3·5 and 5μ) and though the data could be repeated reasonably well (particularly for $\theta_c = 15$ deg) the experimental error is probably about $\pm 0.5\mu$. As can be seen, this represents a wide range of p_b/p_w at the lower end of the test range.

The principal purpose in obtaining these base pressures was to obtain experience of measuring very low pressures. The present results in agreement with data obtained by Kavenau[18], whose careful measurements show that p_b/p_w increases with Re_L. In the middle part of the test range, the base pressure seems to be independent of θ_c. At high values of Re_L out-of-balance effects probably obscure any effect of changes in θ_c; at the lowest test pressures the results seem to indicate, despite the inherent lack of accuracy, that the larger cone has a smaller base pressure. It is not known, however, how much the base pressure is influenced by the large size of the model compared with the isentropic nozzle cone, and more detailed work is needed before an influence of cone angle on base pressure can be accepted.

3.4. Pressure drag.

Because of the higher surface pressures induced by the thick boundary layer, the pressure drag of both sharp-pointed cones should be greater than the corresponding inviscid values. Some reduction in drag, however, will be associated with the strong fall in pressure near the cone trailing edges. The pressure distributions of Figs. 12 and 14 were mechanically integrated to obtain the pressure-drag coefficient of the forward-facing surfaces and, divided by the inviscid pressure-drag coefficient $(C_D)_{ic}$, these results are presented in Fig. 22. A correction has been applied to the results at the three highest values of Re_L in order to compensate for the longitudinal pressure gradient known to exist in the empty tunnel.

The scatter of the experimental results is fairly large (and may perhaps be attributed to difficulties in estimating the pressure distributions near the cone shoulder to the rear of hole 6). Nevertheless for $\theta_c = 15$ deg, there is a marked decrease in the drag ratio as Re_L grows and a similar trend is perhaps evident at $\theta_c = 30$ deg. These experimental curves may be compared with simple theoretical ones derived from considering only the first terms in equations 4a and 4b and integrating these over the entire cone surface. This leads to a drag ratio of the form

$$\frac{C_{D_p}}{(C_{D_p})_{ic}} = 1 + \frac{G}{\sqrt{Re_L}} \tag{5}$$

where G has a different value for the two cones. These theoretical curves exhibit much the same trend as the experimental ones. The latter are lower mainly because of the reduction in drag associated with the upstream effect of the base; the difference between the two curves is in effect an approximate measure of the way the base influence relieves the drag. The most important feature of Fig. 22 however is the large increase in the drag ratio as θ_c reduces from 30 deg to 50 deg.

Ipsen[4,5,6] has measured the total drag of 15 deg half-angle cones at Mach numbers near 2 using a force balance and a support system which eliminates the upstream base effect so significant in the present tests. He shows that the measured drag coefficient may be closely approached by adding together the component drag coefficients arising from the boundary-layer induced pressure and the skin friction. In the latter case the second-order shear due to transverse curvature is very important. Direct comparison between the pressure drag ratios in Fig. 22 and Ipsen's total drag for $\theta_c = 15$ deg is of doubtful value, because to obtain his experimental pressure drag, the large estimated surface friction must be subtracted from a rather larger total drag, with consequent loss in accuracy. For what it is worth the estimates of Ipsen's pressure drag appear to be close to, but a little lower than, the theoretical lines in Fig. 22, a result that might be expected once the base influence has been eliminated.

13

3.3. *Effects of Nose Truncation.*

Successive truncations to the tips of both cones were made subsequently to the completion of the main tests on the pointed cone. The models were cut off normal to their axes; details of the tip geometry are given in Fig. 9 and in Section 2.3. The pressures on the forward-facing surfaces and on the base were measured over the complete range of tunnel pressure on each cone. The scatter was rather more evident during these tests than with the original measurements on the pointed cones.

In general the changes in surface pressure were not large and were in fact negligible for the two most rearward holes (5 and 6) and for the base hole. The variation of base pressure ratio with Re_L is shown for State E (the greatest amount of truncation) in Figs. 21a and b.

The sparseness of the pressure holes and the increased scatter present difficulties in deciding the actual shape of the pressure distributions on the truncated models. Sequences of results with increasing truncation are plotted for the 15 deg cone in Fig. 23a ($p_w = 40\mu$) and Fig. 23b ($p_w = 70\mu$). Both Figures show a strong overexpansion of the flow close to the nose, followed by a smooth recompression back to pressure level of State A. The general effect is smaller at the higher pressure. Similar results for the 30 deg cone are given in Figs. 24a and b, and for this model the influence of the tip truncation is much smaller, probably because of the larger region of subsonic flow to the rear of the bow shock. At $p_w = 70\mu$ for $\theta_c = 30$ deg, it is difficult to distinguish distinctly changes associated with nose bluntness, except for the most forward hole on State C, which is very close to the tip and as a consequence may not give a realistic reading.

The difference between the two cones may be illustrated more clearly by plotting, as in Fig. 25, the pressure-increment parameter against tip truncation at the second pressure hole (which becomes the most forward hole for States D and E). The pressure level at this hole is almost independent of truncation when $\theta_c = 30$ deg, whereas on the more slender model there is a gradual increase in pressure.

A given position on the cone surface will be influenced by two factors which might cause departure from the pointed-cone value. First, the inviscid effect of nose blunting, with its associated expansion and compression, should have a powerful effect near the nose. Secondly, the pressure may change because the boundary layer growth, and hence the magnitude of the viscous interaction effect at a given position, alters with progressive blunting. Indeed these two effects ought not to be regarded as simply superimposed, and must influence each other to some extent. With the present limited data not a lot can be done to distinguish these effects. However, if the boundary layers on the inclined cone surfaces grow from the leading edge in a similar manner to the development on a pointed cone (i.e. the truncation has no effect on the growth) then the viscous interaction effects should depend on Re_s (measured now from the truncated tip). Data for $\theta_c = 15$ deg, at $p_w = 40\mu$ and 70μ, and obtained at pressure holes influenced by the truncation, are plotted against $1/\sqrt{Re_s}$ on Fig. 26. A comparison is made with the curve plotted in Fig. 16a and based on the first term in equation (4a); this curve tends to lie on or below the pointed-cone data. In general, the results for the blunted cones lie below the reference line, suggesting that the boundary-layer growth may be different on the truncated cones and the viscous-interaction effect smaller. This is a somewhat tentative deduction however.

When the tip is blunt the bow shock is detached, and for $\theta_c = 30$ deg, in argon, the two shock shapes for States A and E can be compared in Fig. 27*. Apart from the highly-curved region near the truncated tip, the shock shapes in the two cases are not very different. Even when the cone tip is nominally sharp the bow shock is slightly curved due to the influence of the boundary-layer growth on the cone. If it is accepted that the very small increase in shock angle which exists when argon is used instead of air may be neglected, then the argon afterglow photographs may be used directly. The steepest part of the shock is at an angle of about 56 deg to the stream direction. At a Mach number of 1·90 (the stream Mach number at this downstream position), this is the value obtained in air for a solid cone of semi-vertex angle close to 34 deg. At $x/L = 0.16$, the calculated increase in θ_c due to the boundary-layer growth was 9·2 deg

---

*The model was mounted just downstream of the skirt-exit plane for these photographs in order to avoid optical distortion from the skirt material. The argon glow increases as the pressure rises and hence shock waves show up quite clearly. Expansion regions can be seen as slow gradations of luminosity but are difficult to photograph. The luminosity extends some way into the nozzle or jet boundary layer.

$(\theta_c + \theta_\delta = 39 \cdot 2 \text{ deg})$; this reduces to 4 deg over the rear part of the cone. It is possible then that the initial inclination of the shock does not correspond to that appropriate to the effective cone shape used in estimating the surface pressures. Indeed, if this were so, the effective semi-vertex very close to the nose would exceed 40 deg, the shock detachment angle for these flow conditions. There is little evidence of a well-defined detached shock on the pointed model. The limited size of the isentropic core for the stream pressure at which Fig. 27 was obtained and the use of a monatonic gas makes precise arguments about the significance of the observed shock angles difficult to sustain however.

4. *Concluding Remarks.*

It is clear that the rapid growth of a thick laminar boundary on a cone at supersonic speeds has a marked effect on the surface pressure distribution. The results of the present investigation suggest that this viscous-interaction effect can be estimated reasonably well for cones of moderate and large semi-vertex angles at Mach numbers near 2. Good agreement was obtained between a simple theory, based on a tangent-cone method, and the experimental data, despite obvious limitations in the theoretical approach.

The flow in the region just to the rear of the model has been shown to be similar in many ways to that obtained at high Reynolds number and the measured base pressures agree well with more comprehensive results described by Kavenau in Ref. 18.

The effects of blunting the cone tips were generally small, particularly for the 30 deg cone. There is some evidence that the viscous-interaction effect may be less marked on the truncated cones.

5. *Acknowledgements.*

The manufacture of the models and their installation in the tunnel was carried out by Mr. D. Cooke. Mr. S. Metcalf gave valuable assistance with the experimental work and with the subsequent analysis and discussion.

LIST OF SYMBOLS

d	External diameter of probe
d_i	Internal diameter of probe
p	Measured pressure on forward-facing cone surfaces
p_{ic}	Cone surface pressure in inviscid flow
p_b	Measured base pressure
p_t	Test-chamber pressure
p_w	Nozzle pressure upstream of exit plane
r_b	Radius at cone base
r_s	Radius at position s
s	Distance along cone surface from vertex
x	Distance along cone axis from vertex
A', B', A, B, D, G, K	Numerical constants
C	Chapman-Rubesin factor relating viscosity and temperature changes
C_D	Pressure-drag coefficient for forward-facing surfaces
$(C_D)_{ic}$	Value of C_D in inviscid flow
H_0	Total pressure of flow
H_1	Total pressure behind normal shock in ideal flow
H'_1	Measured pitot pressure
K_T	Knudsen number, based on tip diameter (equal to $1 \cdot 51\, M_0/Re_T$)
L	Cone length from vertex to base ($1 \cdot 25$ inches)
M_0	Free-stream Mach number
M_s	Local Mach number at position s
Re_d	Reynolds number based on free-stream conditions and probe external diameter
Re_L	Reynolds number based on free-stream conditions and cone length L
Re_s	Reynolds number based on surface distance s and local conditions at outer edge of boundary layer
Re_T	Reynolds number based on stream conditions and diameter of blunt tip
T_0	Stagnation temperature of flow
α	Flow deflection at rear of cone
δ^*	Boundary-layer displacement thickness
θ_c	Semi-vertex angle of cone
θ_δ	Effective angle of boundary-layer growth
μ	Pressure equal to one micron of mercury
χ	Hypersonic similarity parameter, equal to $\sqrt{C}\, M^3/\sqrt{Re}$

REFERENCES

No.	Author(s)	Title, etc.

1 L. Talbot

Viscosity correction to cone probes in rarified supersonic flow at a nominal Mach number of 4.
NACA TN.3219 (November, 1954).

2 R. F. Probstein

Hypersonic flow theory.
Section 9.2 pp. 351 – 353
Academic Press 1959.

3 L. Talbot, T. Koga and P. M. Sherman..

Hypersonic viscous flow over slender cones.
NACA TN.4327 (September, 1958).

4 D. C. Ipsen

Cone drag in a rarefied gas flow.
Univ. Calif. Report HE–150–114. (August, 1953).

5 D. C. Ipsen

New experiments on cone drag in a rarefied gas flow.
Univ. Calif. Report HE–150–127. (April, 1955).

6 D. C. Ipsen

Experiments on cone drag in a rarefied air flow.
Jet Propulsion, *26*, pp. 1076–1077. (December, 1956).

7 R. F. Probstein and D. Elliott

The transverse curvature effect in compressible axially symmetric laminar boundary-layer flow.
J. Ae. Sci. 23, pp. 208–224 and 236. (March, 1956).

8 K. R. Enkenhus

The design, instrumentation and operation of the UTIA low-density tunnel.
UTIA Report No. 44. (June, 1957).
A.R.C. 21147.

9 R. K. Sreekanth

Performance of a Mach 4 axially symmetric nozzle designed to operate at 40 microns Hg in the UTIA low-density wind tunnel.
UTIA TN. No. 10. (September, 1956).

10 W. B. Kunkel and F. C. Hurlbut

Luminescent gas flow visualization for low-density wind tunnels.
J. of App. Phys. Vol. 28, 00. 827–835. (August, 1957).

11 K. R. Enkenhus

Pressure probes at very low density.
UTIA Report No. 42. (January, 1957).

12 F. S. Sherman ..

New experiments on impact-pressure interpretation in supersonic and subsonic rarefied air streams.
NACA TN.2995. (September, 1953).

13 L. Rosenhead (Ed.)

A selection of graphs for use in calculations of compressible air flow.
Oxford University Press (1954).

14 W. D. Hayes and R. F. Probstein

Hypersonic flow theory, Section 9.2, p. 343.
Academic Press (1959).

REFERENCES—*continued*

No.	Author(s)	Title, etc.

15 W. Mangler .. .. .. Zusammenhang zwischen ebenen und rotationssymmetrischen Grenzsichten in kompressiblen Flüssigkeit.
Z.A.M.M. *28*, pp. 97–103 (1948).

See also:—

L. Howarth (Ed.) .. .. *Modern Developments in Fluid Dynamics*, Vol. 1, p. 382 et seq.
Oxford University Press (1953).

16 R. F. Probstein and .. .. Hypersonic similarity and the tangent-cone approximation for unyawed bodies of revolution.
K. N. C. Bray .. .. .. *J. Ae. Sci. 22*, pp. 66–68 (January, 1955).

17 E. W. E. Rogers, C. J. Berry and Tests at transonic speeds on wings with wedge sections and sweep varying between 0 deg and 60 deg. A.R.C. R. & M. 3348 (October, 1961).
V. G. Quincey .. .. ..

18 L. L. Kavenau .. .. .. Base pressure studies in rarefied supersonic flows.
J. Ae. Sci. 23, pp. 193–207 & 230. (March, 1956).

APPENDIX

Tunnel Instrumentation and Manometers.

A1. *Instrumentation.*
The following instruments are used to measure the basic tunnel pressures:

A1.1. *McLeod Gauge.*
This is the primary standard for all pressure measurements up to 1 mm. It has a bulb volume of 500 cc, a capillary diameter of 0·4 cm and a closed limb length of 20 cm. It has compression ratios of 4000, 2000, 1000, 500 and 250. The mercury is raised and lowered by needle valves in vacuum and atmospheric pressure lines. The glassware is joined to the stainless-steel reservoir by a ground-glass socket to stainless-steel cone. A liquid nitrogen cold trap prevents migration of mercury from the gauge.

A1.2. *Alphatron Gauge.*
This is the Model 520 manufactured by N.R.C. Equipment Corporation. It is connected to the same chamber-pressure line as the McLeod and gives a continuous indication of p_t.

A1.3. *Oil Manometer.*
This uses 'Apiezon *A*' vacuum pump oil as the manometer fluid. It is possible to read the meniscus displacement with a travelling microscope to within 0·001 in. ($1·68\mu$). This is not its accuracy, however, as there is some zero instability which has not yet been resolved. It is used to measure stagnation pressure (H_0) and frequent checks against the McLeod gauge show that this pressure is now being read to within $\pm 3\mu$. The reservoir pressure for the oil manometer is maintained at less than $0·1\mu$ by a small vacuum diffusion pump.

A2. *Thermistor Manometer for Measuring Model Pressures.*
When measuring surface pressures with a system involving small-bore tubing and small pressure holes (unavoidable with low-density tunnel models) it is necessary to keep the length of pressure leads and volume of gauge heads to a minimum in order to obtain reasonable response times.

Thermistors are thermally-sensitive resistors whose temperature coefficient of resistance is negative and typically 4 per cent per deg C at 20 deg C. One of the many forms which are available is a small bead about 0·020 in. diameter mounted in a glass tube of 0·15 in. diameter. This form has a thermal time constant of only $1\frac{1}{2}$ seconds. Attempts to mount two thermistors, one as a pressure sensor and the other sealed off as a temperature compensating element, directly in the model failed. Connected as a simple bridge network the compensation for temperature changes was inadequate.

In the system now used the sensing thermistors are mounted in a tube (or bank) through which water is passed from an external tank with the water temperature controlled to within $\pm 0·1$ deg C. This bank is placed as close to the model as possible. The compensating thermistors are no longer required and are replaced by variable resistances. The circuit is shown in Fig. A.1. Setting up is done with the thermistor at a pressure within the proposed operating range. The current in both arms is monitored and set to 2·5 mA by adjusting R_1 and R_2 equally and R_c to get the final equality of current R_c will then be at the operating resistance of the thermistor. With the STC Type A14 now being used this gives a resistance of about 1700Ω, operating temperature of 80 deg C and power dissipation of 10 mW. The required range and sensitivity can be obtained by adjusting R_s. Zero shift is easily done by altering R_c. If $R_s = 10 R_1 = 100 R_c$ only 55 volts D.C. would be required. However, to enable a highly-stabilized power supply to be used and operated at its optimum output of 200V, R_1 and R_2 have been increased to 100kΩ. Bridge output is measured with a Scalamp galvanometer with sensitivity set at 0·6mV for full-scale deflection of 14 cms. At the moment this equipment can measure up to 12 pressures at a time and a typical calibration is shown in Fig. A.2.

The problem in the use of thermistors is the zero drift. It has been found that some drift more than others to an extent where thermistors from the same batch may vary from little drift to an intolerable amount. In some applications it is possible to reset the zero periodically at some known pressure, usually the lowest pressure of the tunnel when the initial calibration will be repeated quite well. Alternatively, frequent calibrations can be done and this is more usual when changes of range are required associated with variations in the test chamber pressure p_t. If provision can be made to overrun the thermistors for a short while at say 10 mA this helps to shorten the daily settling down period; most of the drift occurs during the first hour or so.
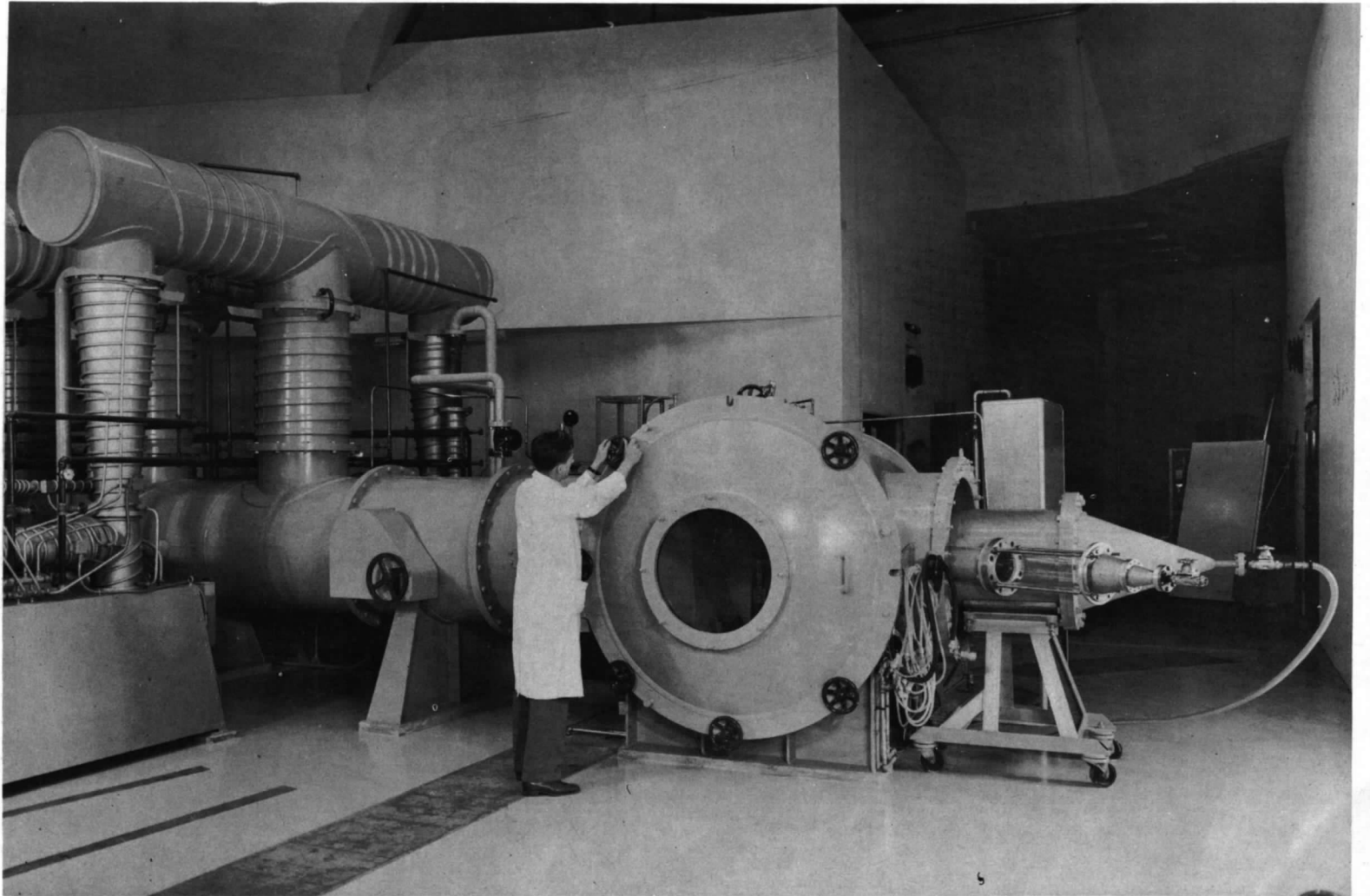
FIG. 1a. N.P.L. low-density tunnel.
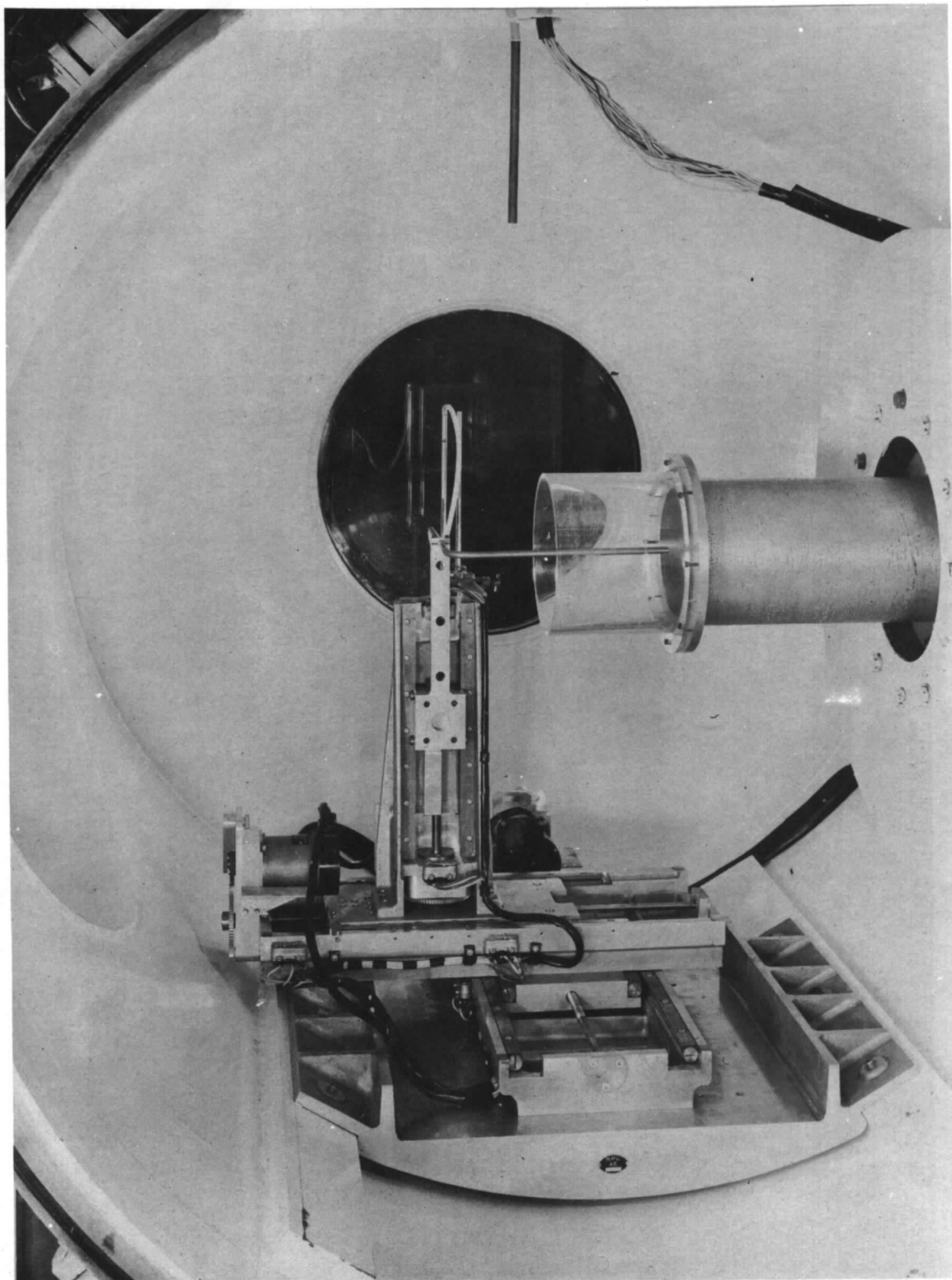
FIG. 1b. View inside test chamber, showing nozzle, plastic skirt and traverse gear with $\frac{3}{8}$ in. diameter pitot probe.
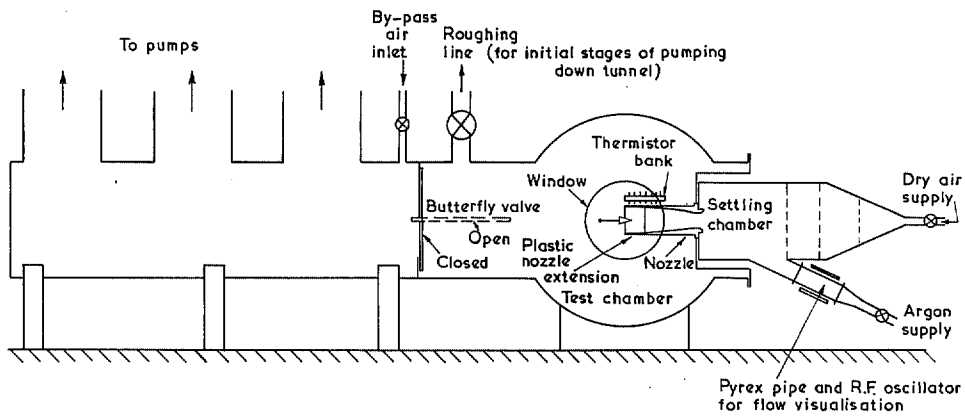
FIG. 2. Diagram of N.P.L. low-density tunnel.
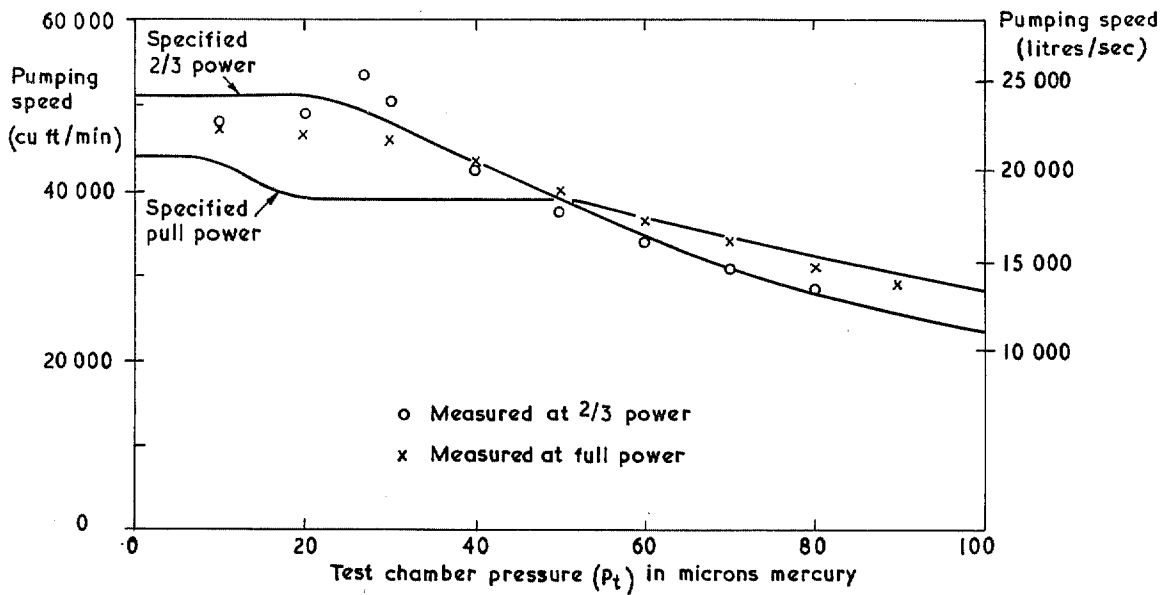
FIG. 3. Pumping speed of five 30B4 vapour booster pumps.
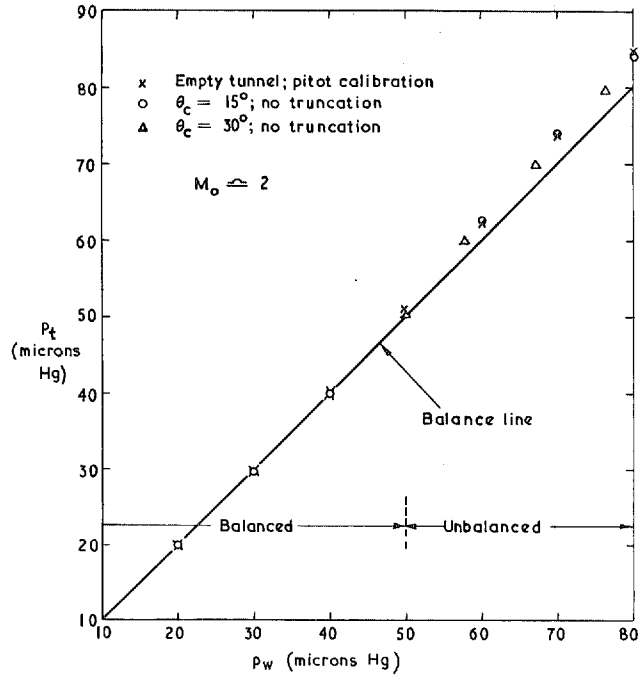
FIG. 4. Pressure balance obtained between nozzle wall hole (p_w) and test chamber pressure (p_t).
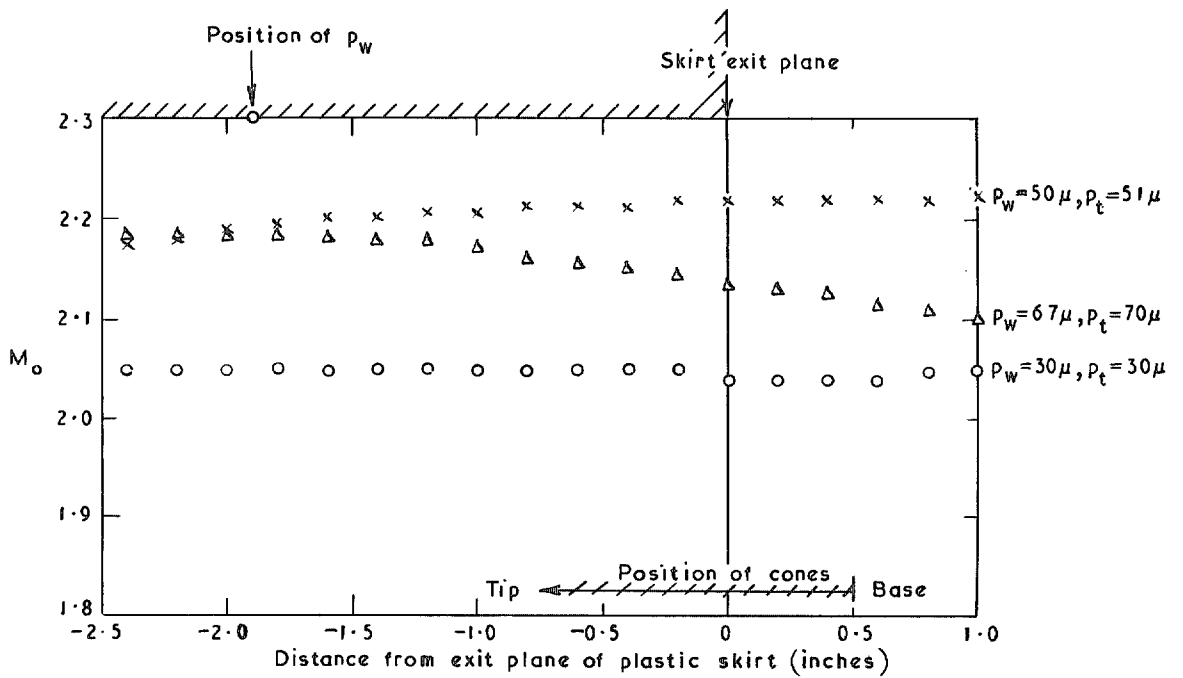
FIG. 5a. Examples of empty-tunnel pitot-tube calibrations along tunnel axis.
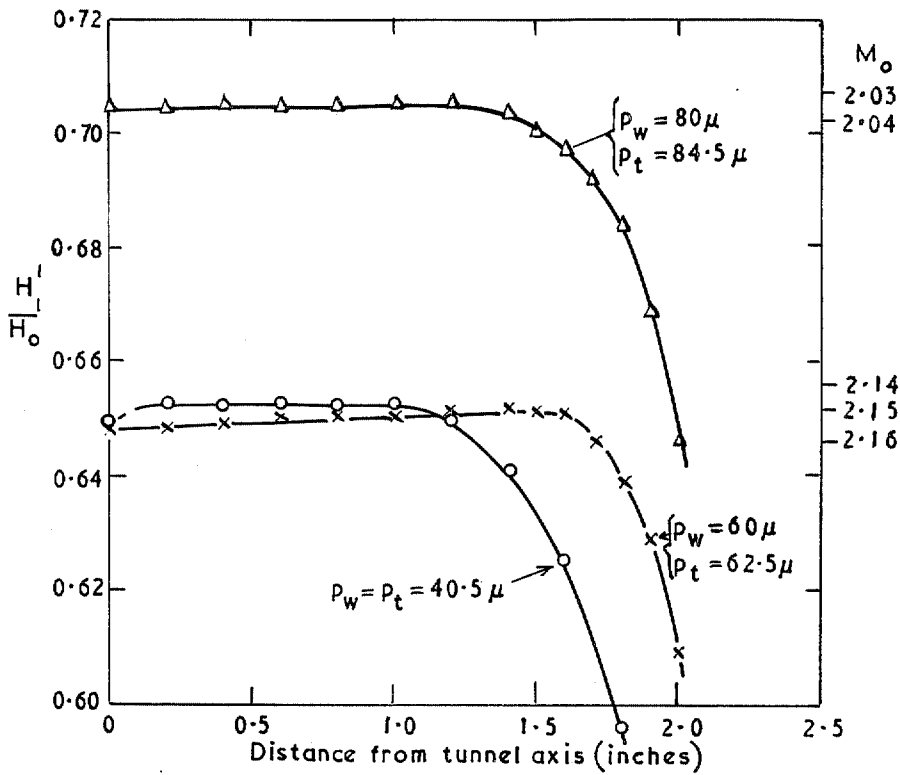
FIG. 5b. Typical transverse flow characteristics at skirt exit plane ($\frac{3}{8}$ in. dia. pitot).
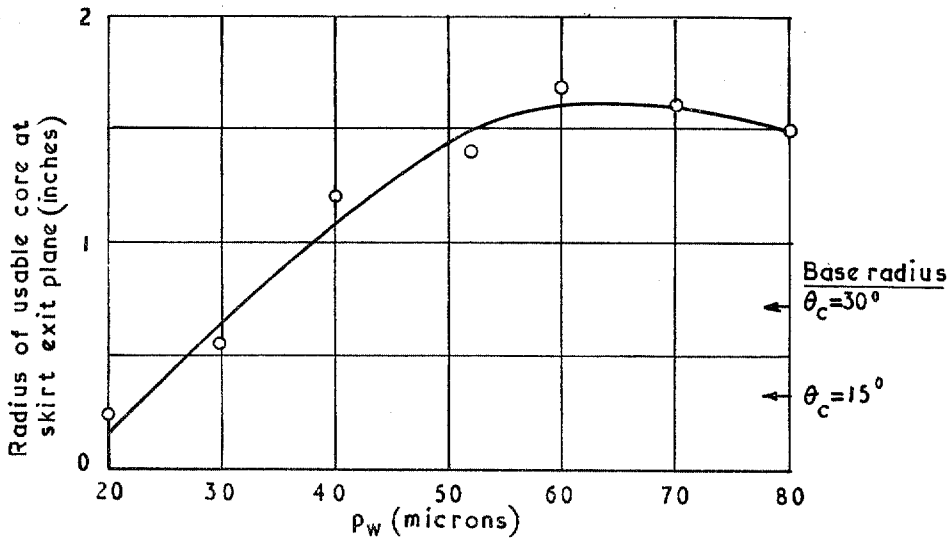
FIG. 5c. Radius of usable core at exit plane.

(Edge of core is defined as station where loss of pitot pressure in nozzle boundary layer exceeds 0·5 per cent H_0).

25
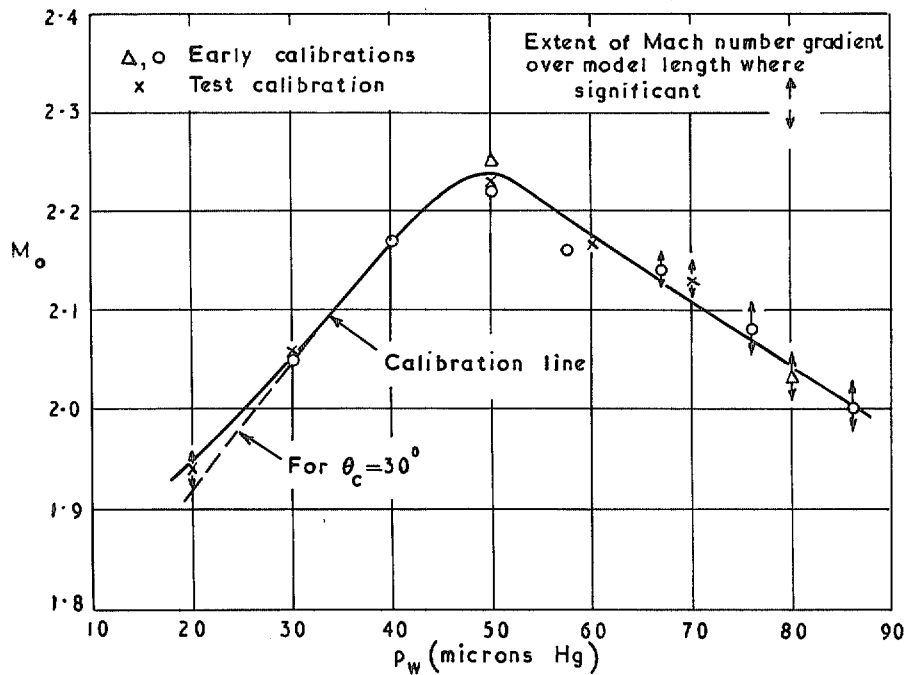
FIG. 6.   Flow Mach number at middle of model, from $\frac{3}{8}$ in. diameter pitot explorations.
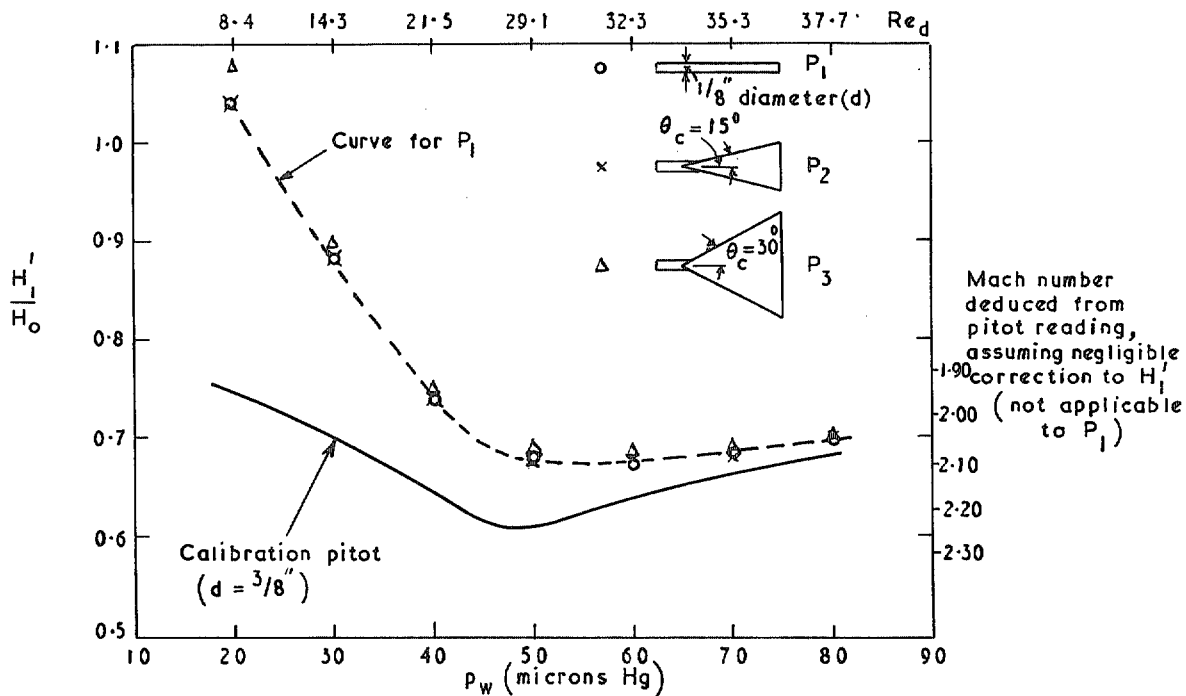
FIG. 7.   Results of investigation of model blockage on test Mach number.
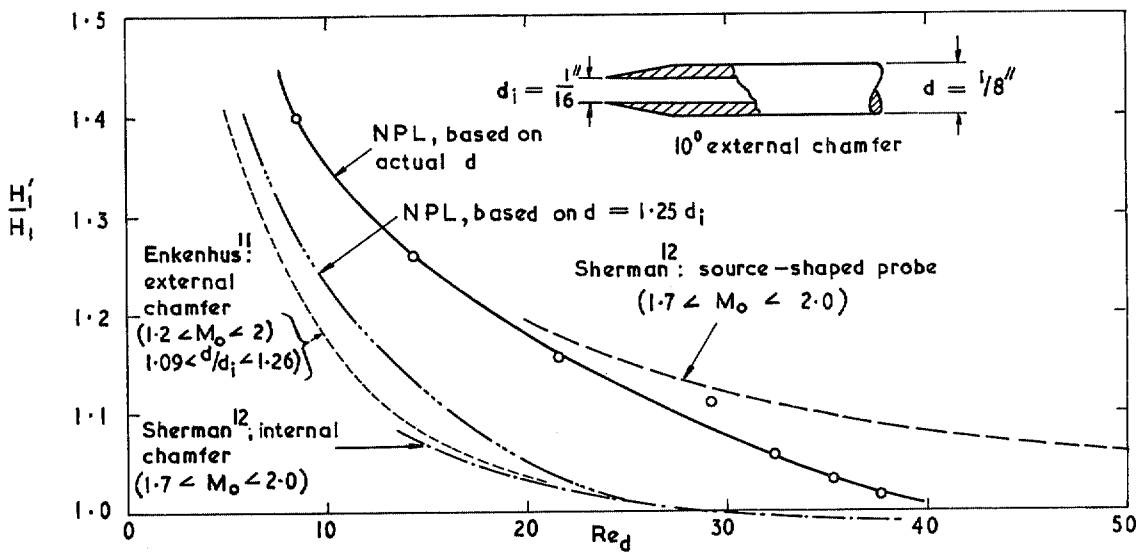
FIG. 8a.   Apparent calibration of $\frac{1}{8}$ in. diameter sharp-edged pitot tube ($M_0 \simeq 2$).
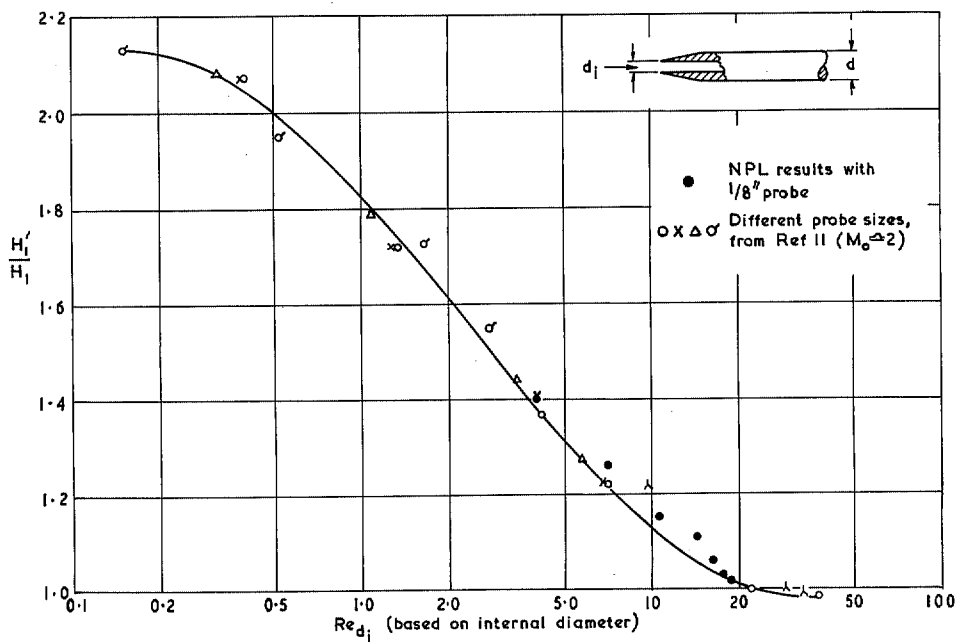
FIG. 8b.   Correlation of probe characteristics based on orifice size.

(a) $\theta_c = 15^0$

Nose positions for various states

(b) $\theta_c = 30^0$
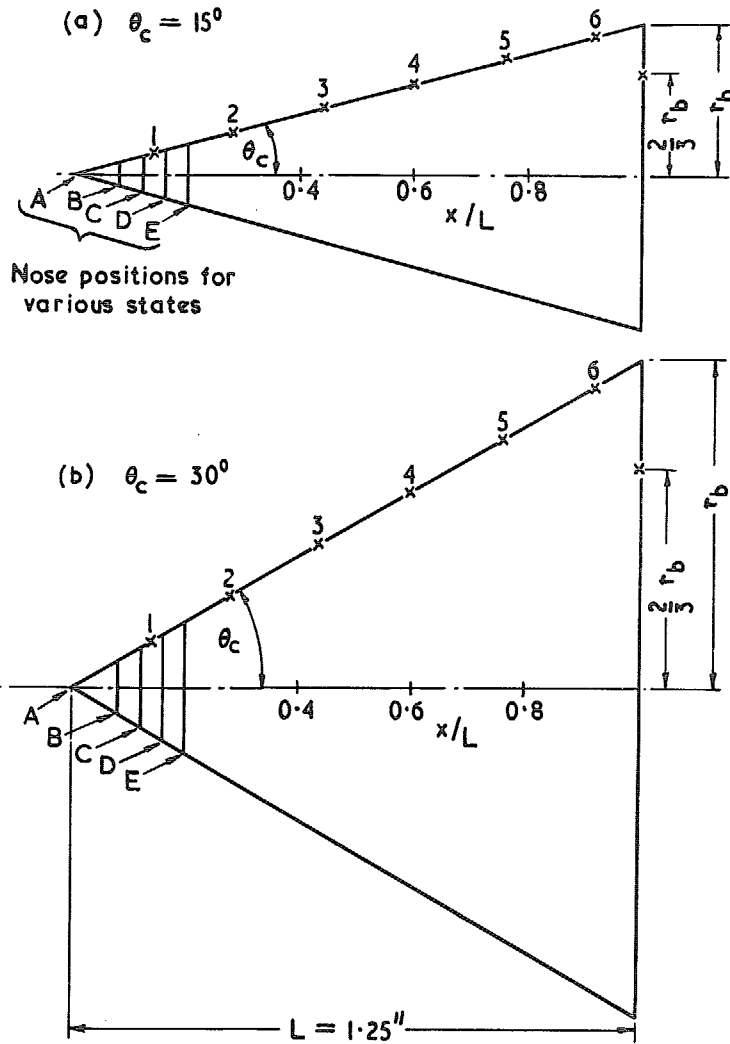
$L = 1.25''$

All hole diameters are $0.010''$

FIG. 9.   Models used for tests on cones
($L = 1.25$ in.).

For $T_0 = 283^0$ K and isentropic flow

Re/inch/micron Hg
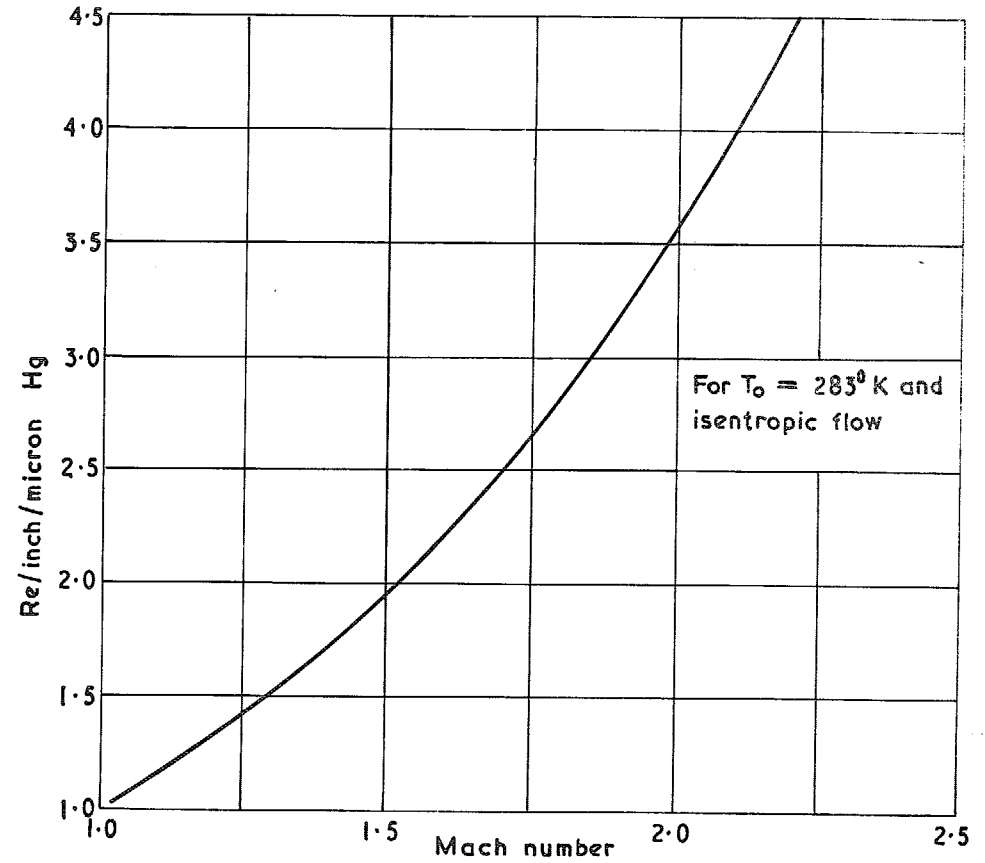
Mach number

FIG. 10.   Variation of flow Reynolds number
with Mach number (based on data in Ref. 8).
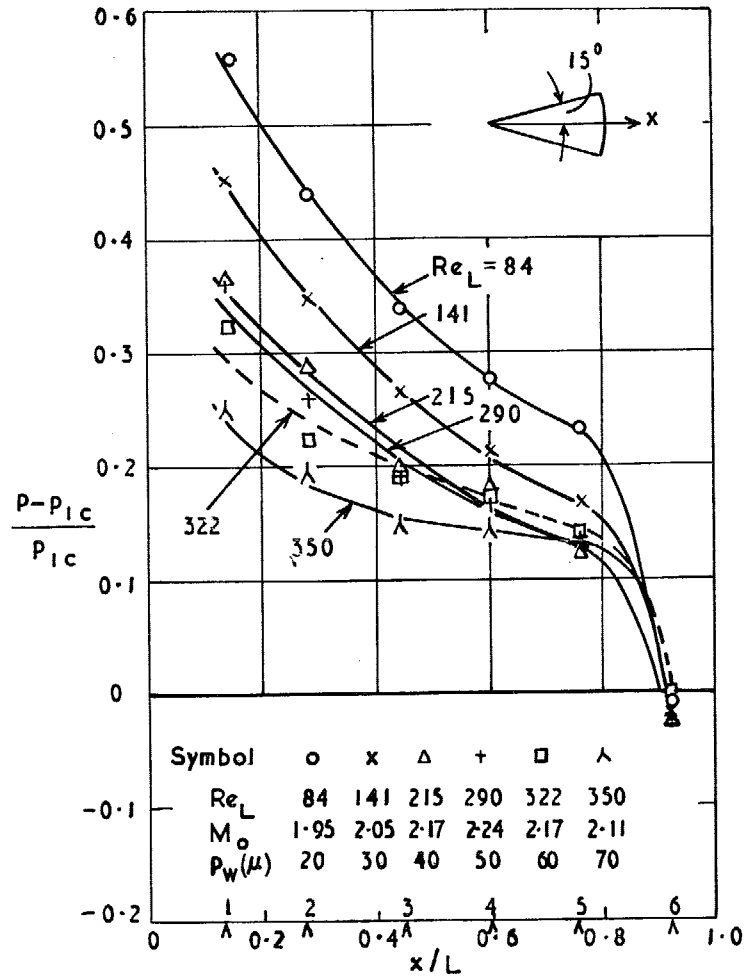
FIG. 11. Influence of test Reynolds number on the viscous-interaction effect for the 15 deg cone. (N.B. data for $p_w = 80\mu$ not plotted).

Symbol	o	x	△	+	□	ʌ
Re_L	84	141	215	290	322	350
M_o	1·95	2·05	2·17	2·24	2·17	2·11
$p_w(\mu)$	20	30	40	50	60	70
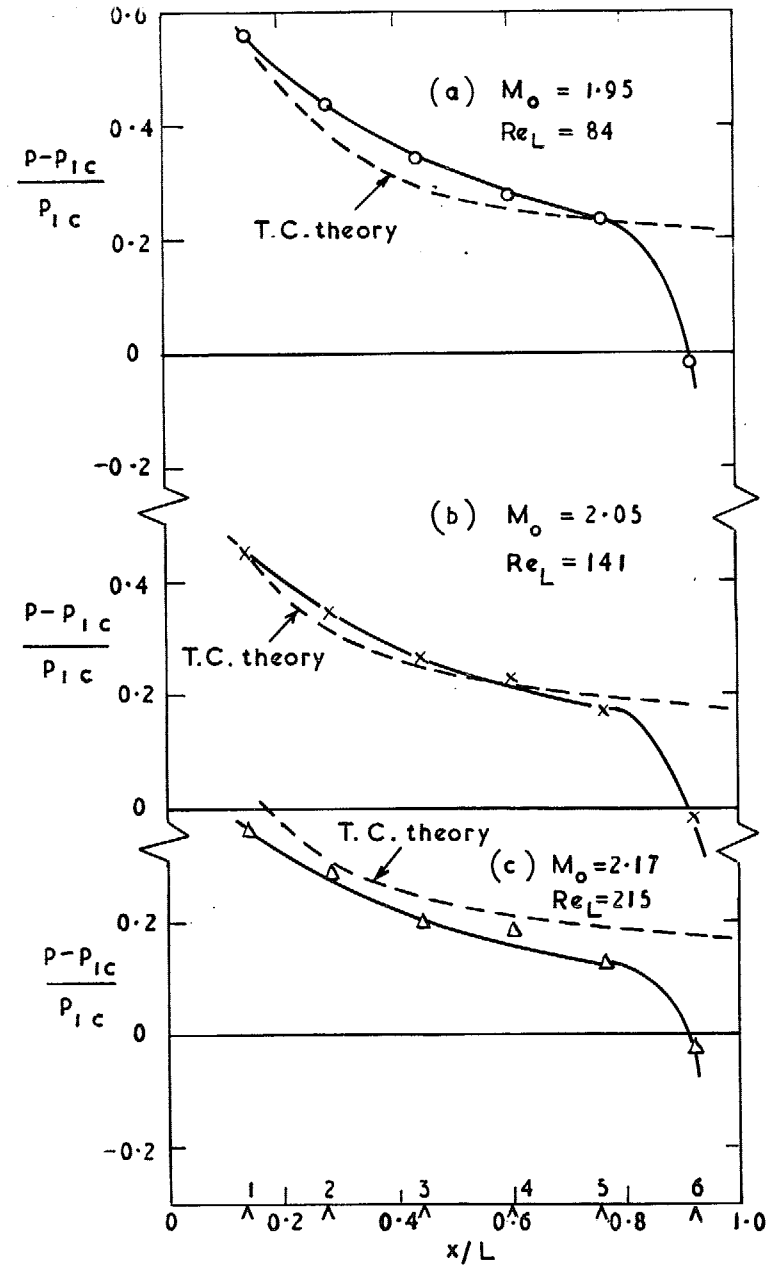
FIG. 12. Surface pressure distributions for the 15 deg cone.
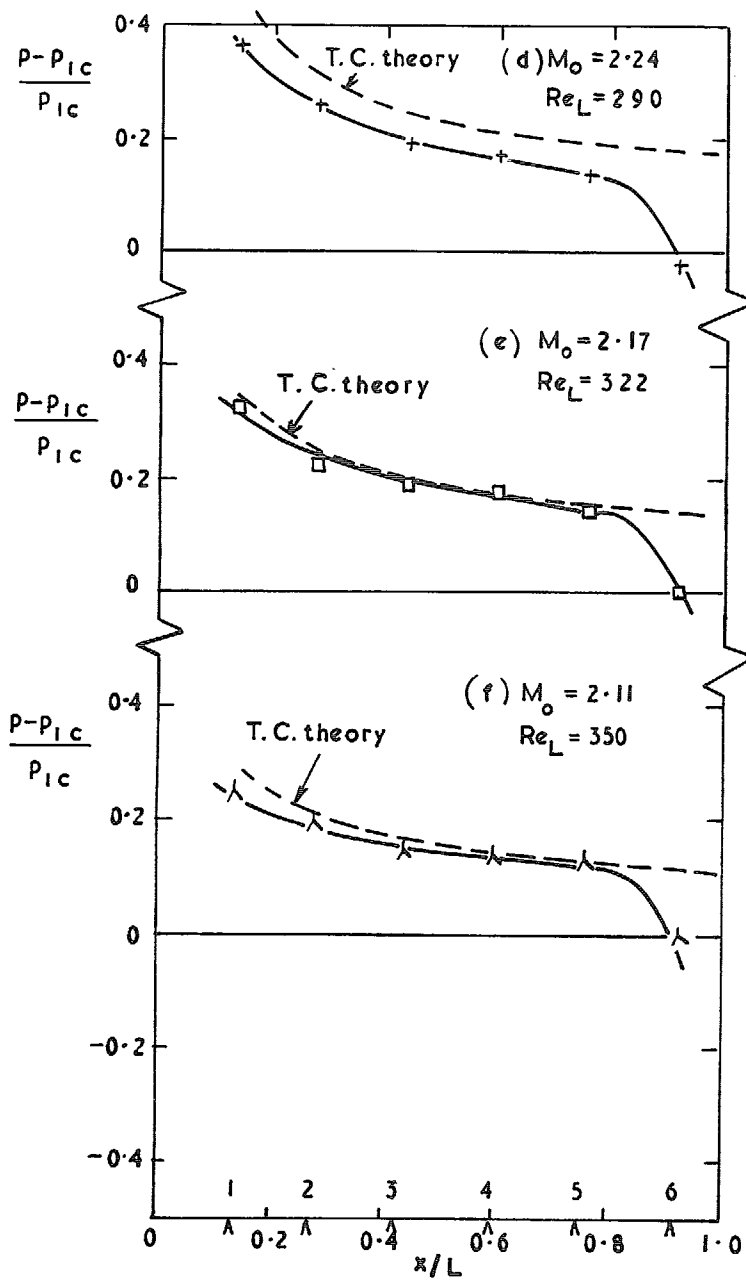
FIG. 12 (contd.).   Surface pressure distributions for the 15 deg cone.
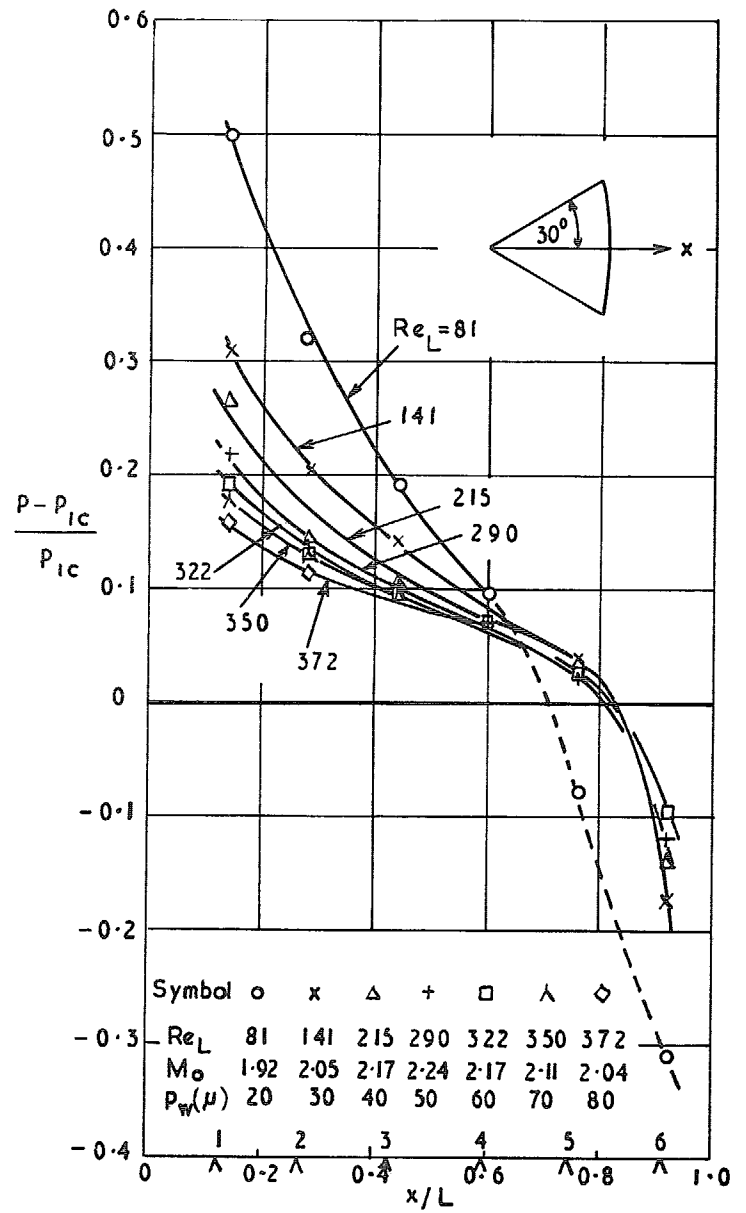
FIG. 13.   Influence of test Reynolds number on the viscous-interaction effect for the 30 deg cone.

(N.B. At $Re_L = 81$, holes 5 and 6 are outside the
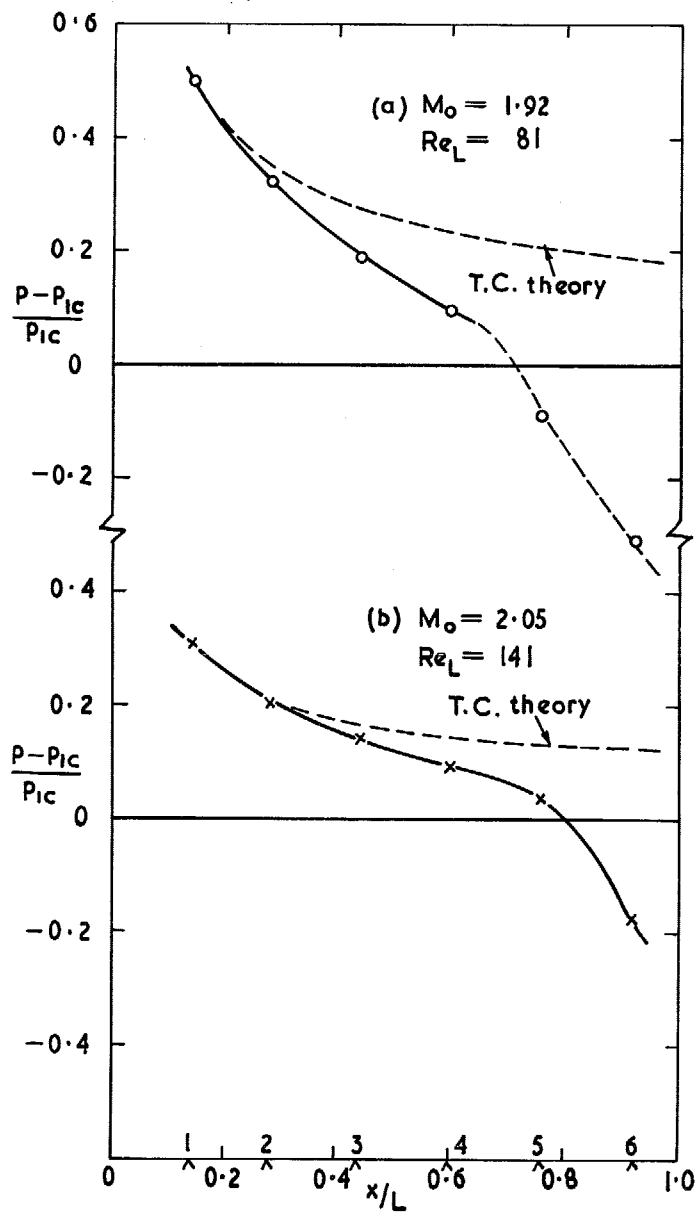
FIGS. 14 (a & b). Surface pressure distributions
for the 30 deg cone.
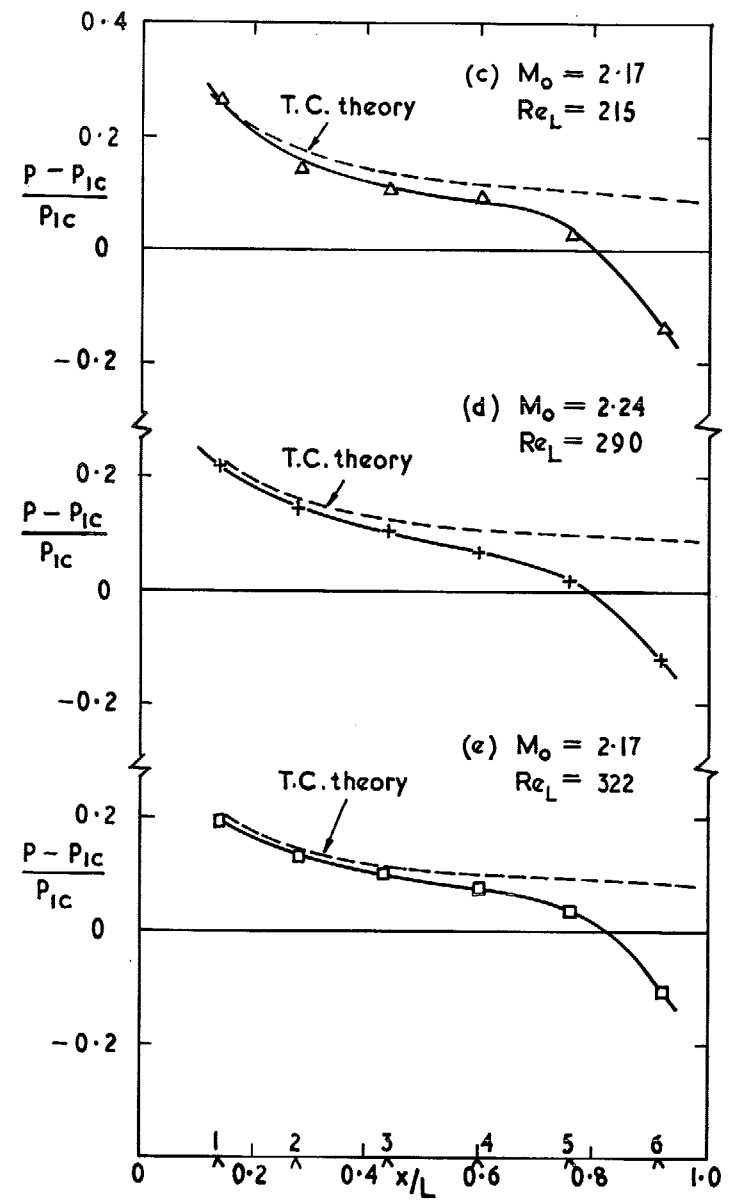
FIGS. 14 (c to e). Surface pressure distributions
for the 30 deg cone.
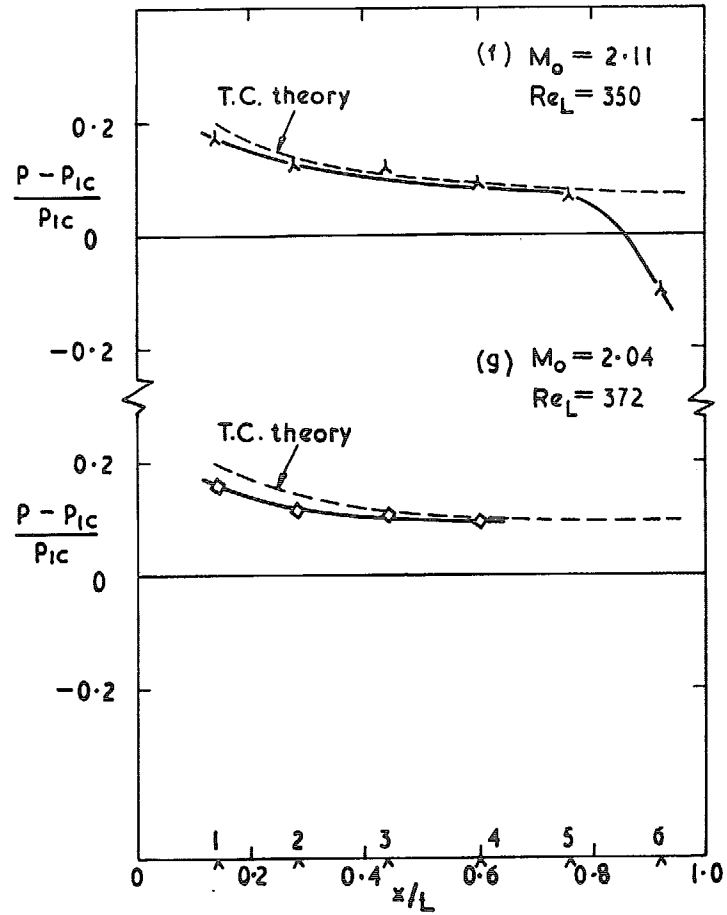
FIGS. 14 (f & g). Surface pressure distributions for the 30 deg cone.
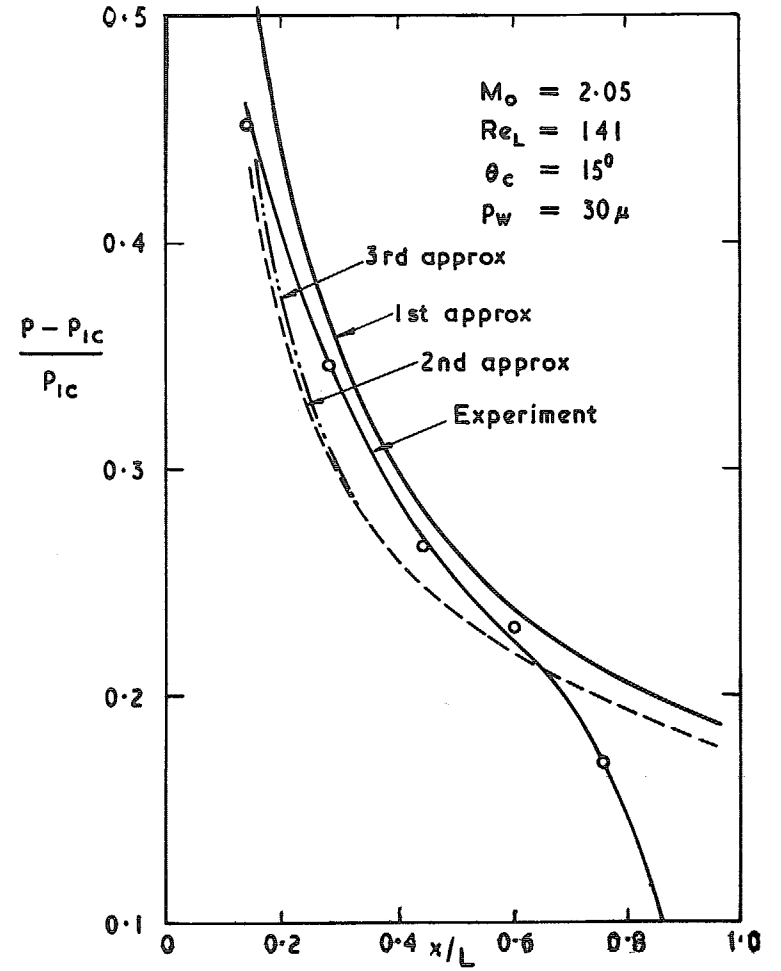
FIG. 15. Illustration of convergence of successive approximations used in tangent-cone theory.
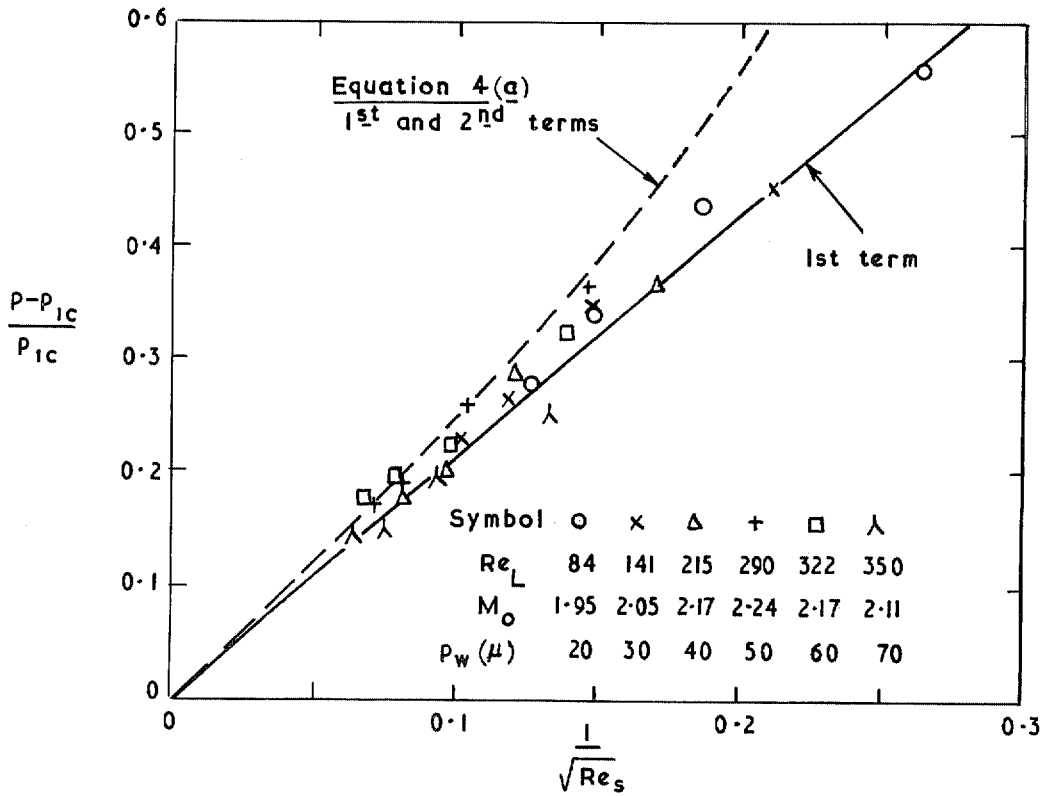
FIG. 16a. Dependence of induced-pressure parameter on local Reynolds number for 15 deg cone.
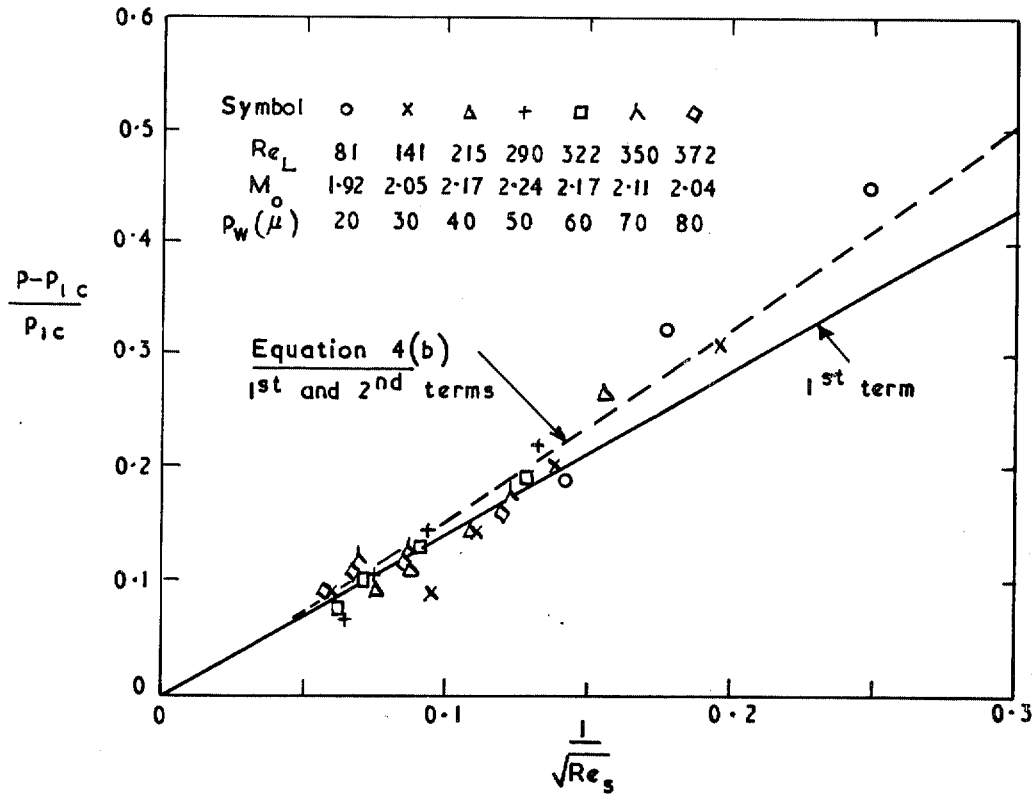
FIG. 16b. Dependence of induced-pressure parameter on local Reynolds number for 30 deg cone.

33
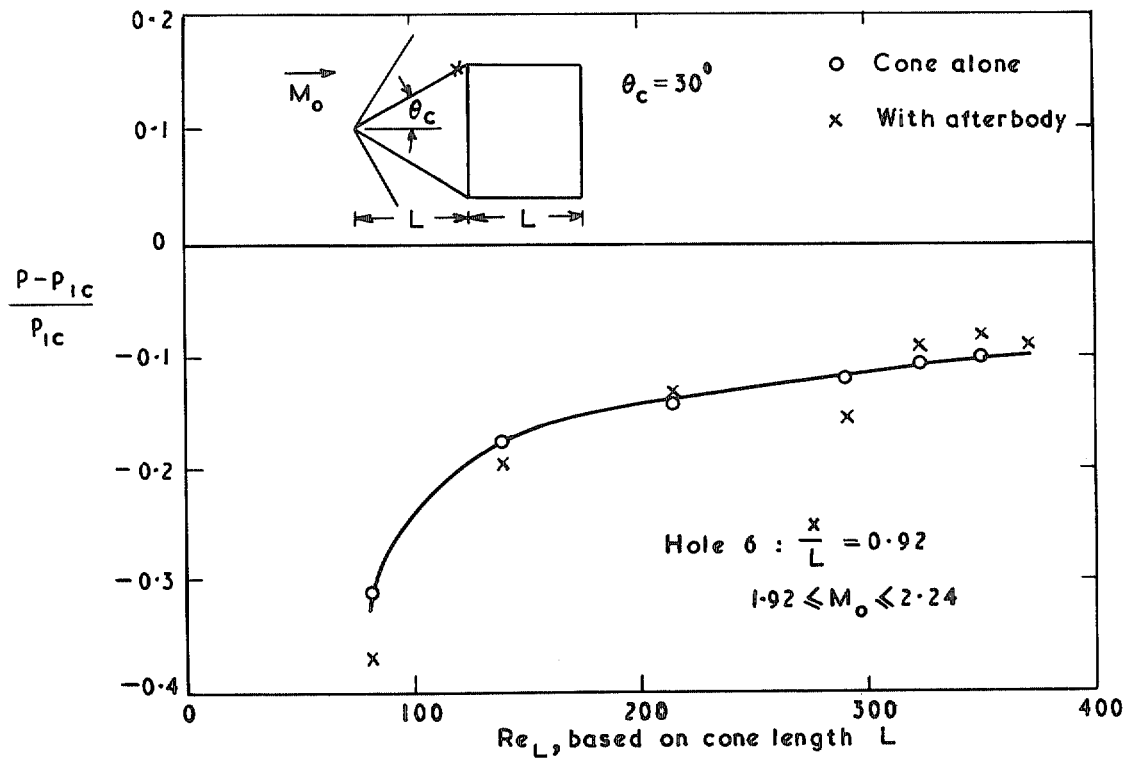
FIG. 17.   Effect of adding afterbody to surface pressure at hole 6.
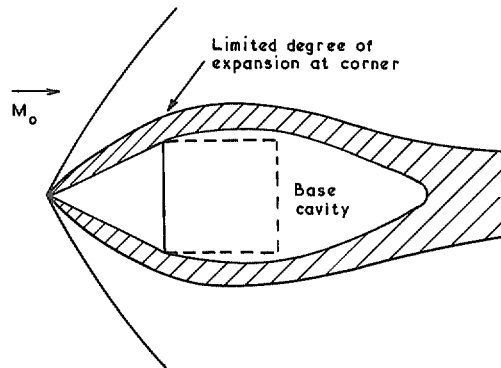
FIG. 18a.   Possible flow in wake of model (cone and cone-cylinder).
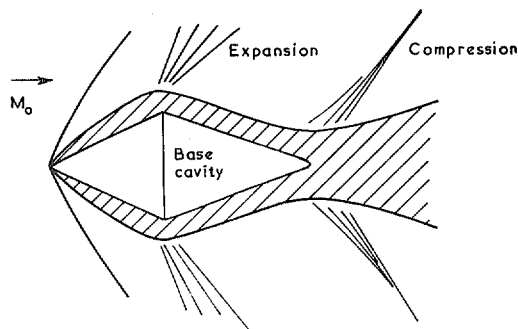
FIG. 18b.   Alternative flow in base region (cone only).

34

Distance from cone base (inches)

$H_1' = 250\mu$ ———————————————— 250μ

300 ———————————————— 300

350 ———————————————— 350

400 ———————————————— 400
450

450 ———————————————— 450

500 ———————————————— 500

Traverse positions shown thus T ↓

Vertical scale (inches)

Edge of central core for empty tunnel

H_1'	Approx M
580	1·72
560	1·79
540	1·85
520	1·92
500	1·98
480	2·04
460	2·11
440	2·17

500 —— 500

500

A → 550

$H_o = 672\mu$
$P_W = 80\mu$

$M_o = 2·04$

Shock for $\theta_c + \theta_\delta = 20°$

$\theta_c = 15°$

550
500

550
500

500 A'

500
450
400
350
300
250
200
190
180

Approximate boundary — layer growth

FIG. 19a.   Wake field at 80μ stream static pressure, showing contours of equal pitot pressure.
Full lines are contours at 50μ spacing.

Distance from cone base (inches)

0   1   2   3

Traverse positions →T   T   T   100 μ

100μ 120

120   140

140   160

Vertical scale (inches)   160   180

180

H_1' Approx M

220   1·87
200   2·02
180   2·18

190

180   190

$M_o = 2·05$

$P_W = 30\mu$

$H_o = 248\mu$ A →

200   ←— A'

200

190 180

170 160

140

120

100

Shock for $\theta_c + \theta_\delta = 20°$

Shock observed in flow visualisation at $p_W \simeq 23\mu$

$\theta = 15°$

90

Approximate boundary-layer growth
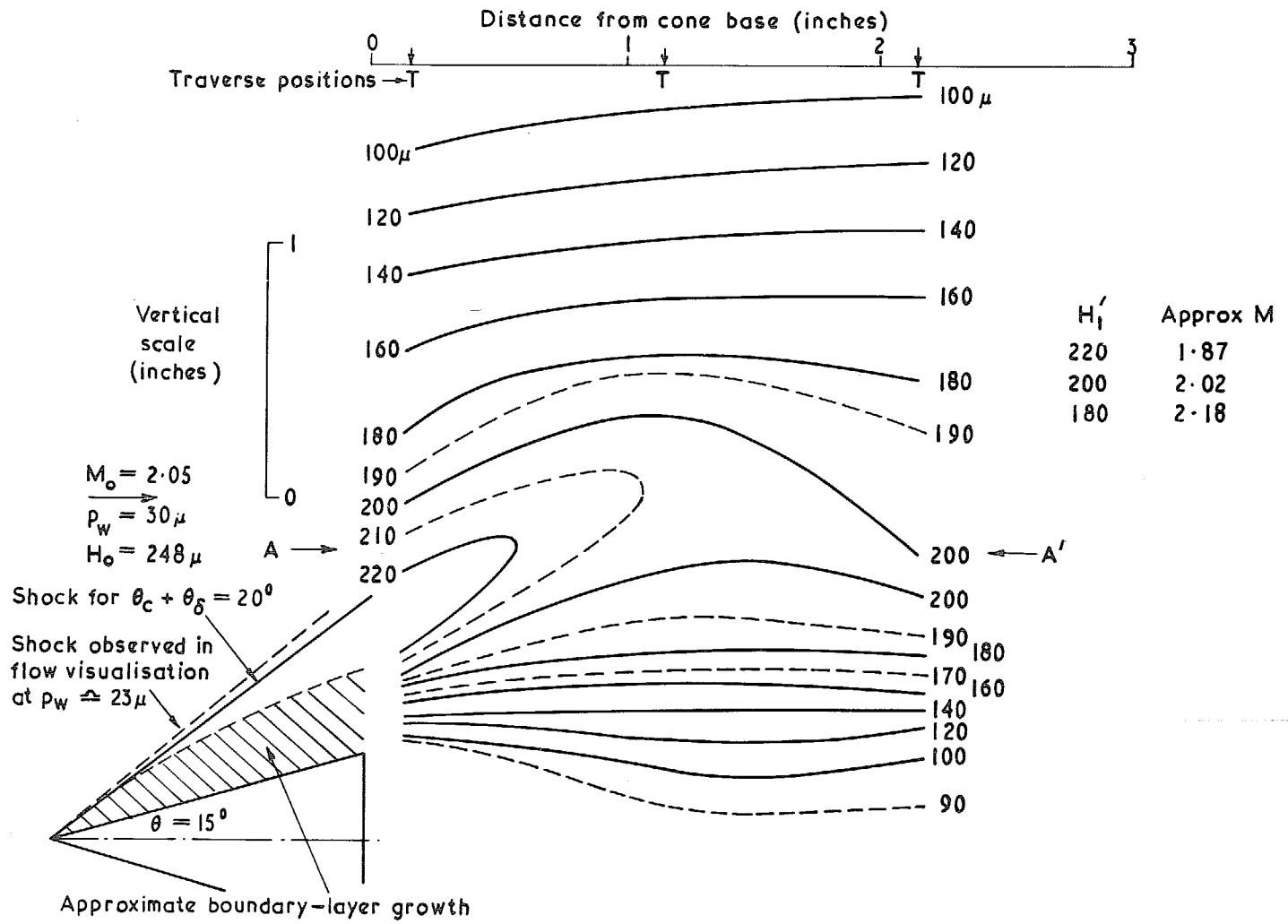
FIG. 19b.   Wake field at 30μ stream static pressure, showing contours of constant pitot pressure.
Full lines are contours at 20μ spacing.

36
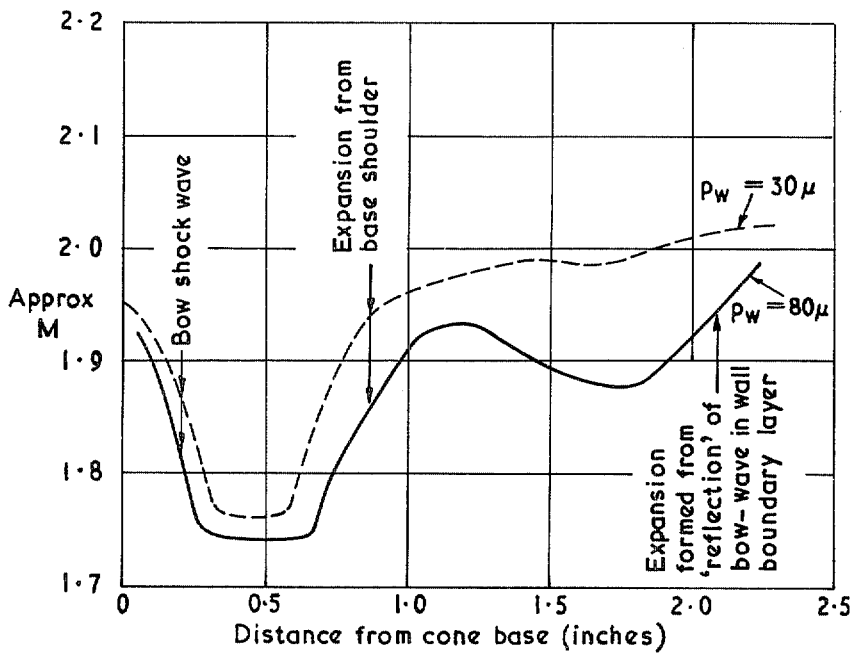
FIG. 20a. Comparison of longitudinal Mach number variation for two test conditions. (Along lines AA' in Figs. 19 (a & b) 0·8 in. above cone shoulder).
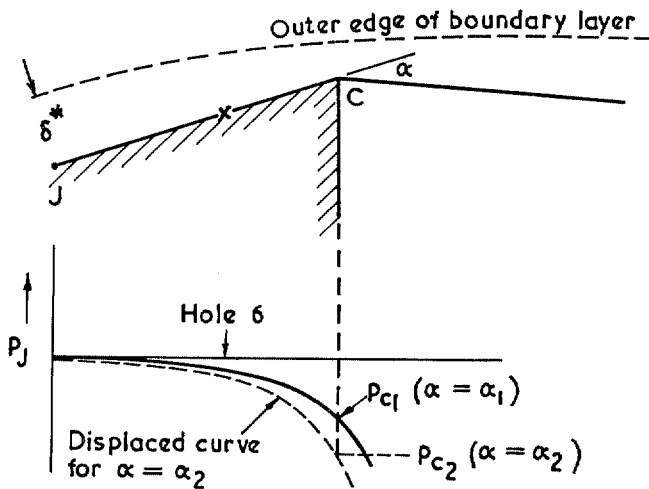
FIG. 20b. Diagram of boundary-layer flow near cone shoulder.
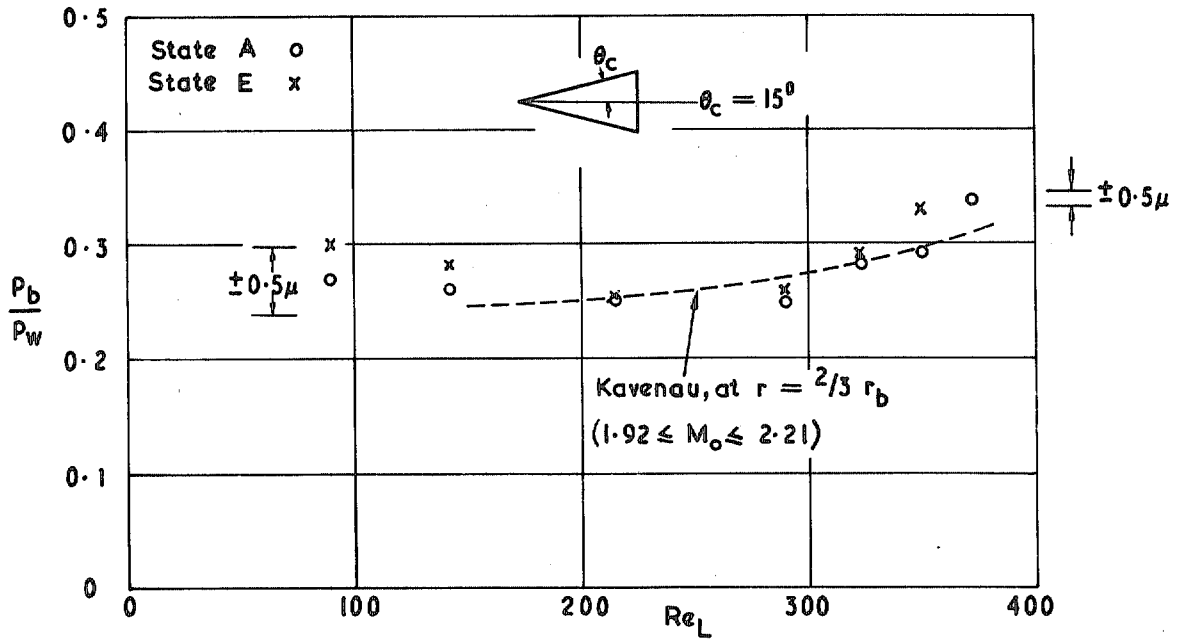
FIG. 21a. Base-pressure ratio for 15 deg cone.
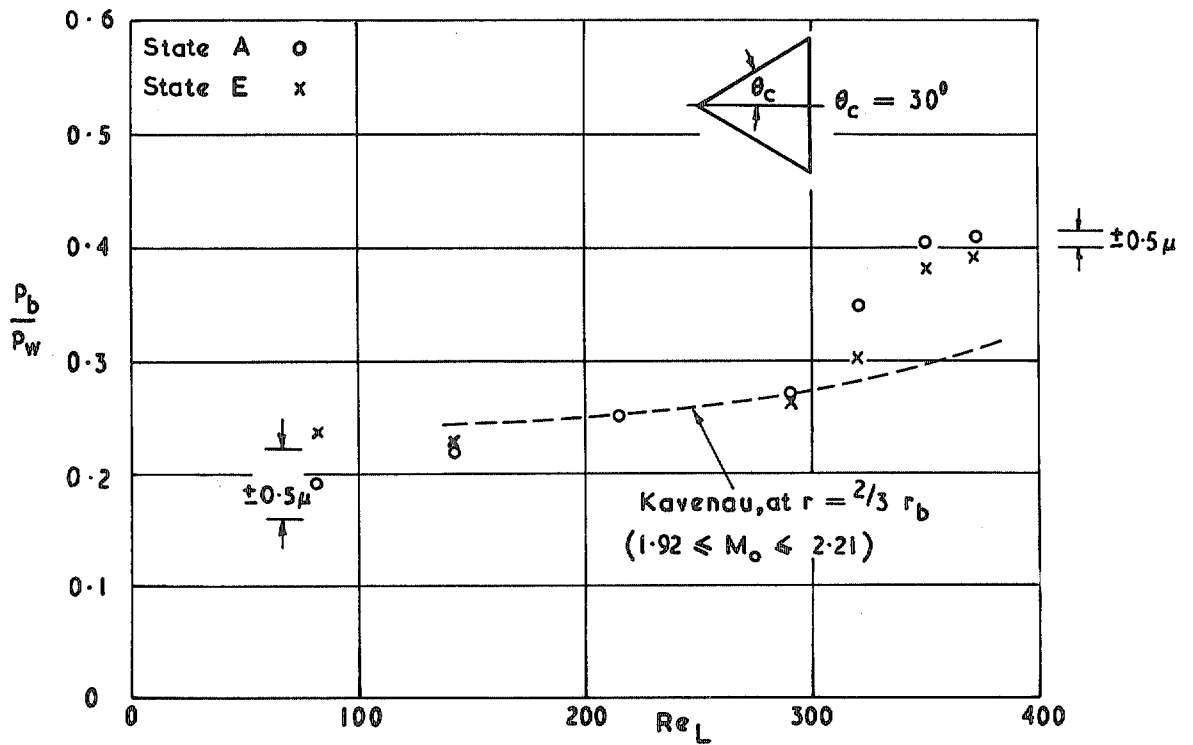
FIG. 21b. Base-pressure ratio for 30 deg cone.
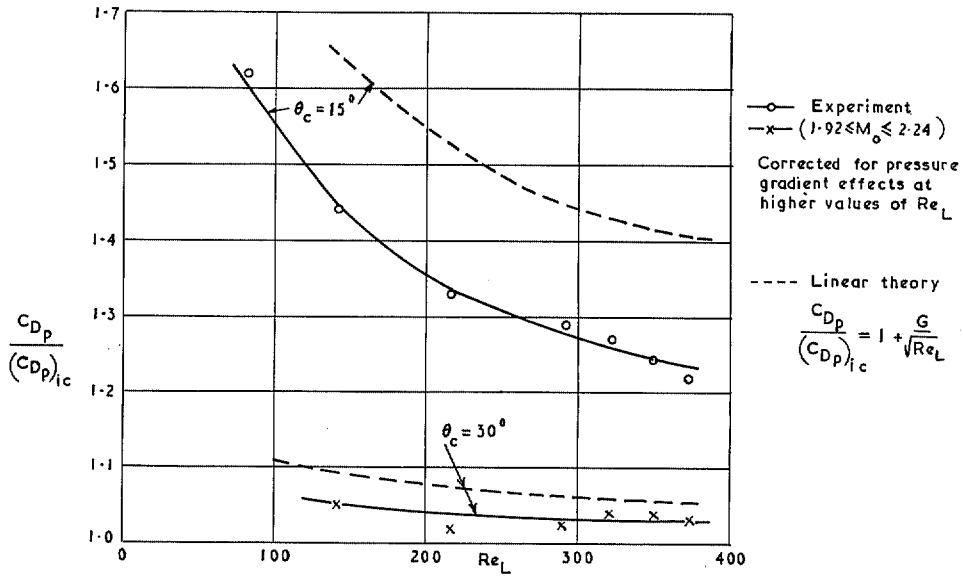
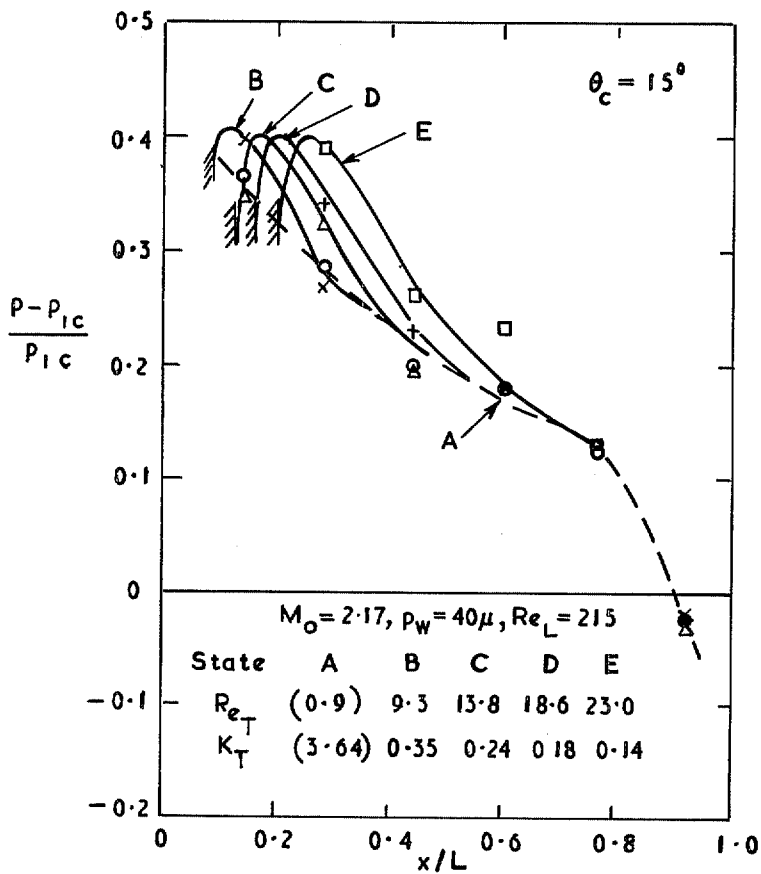FIG. 22.   Increase in pressure drag due to viscous effects.

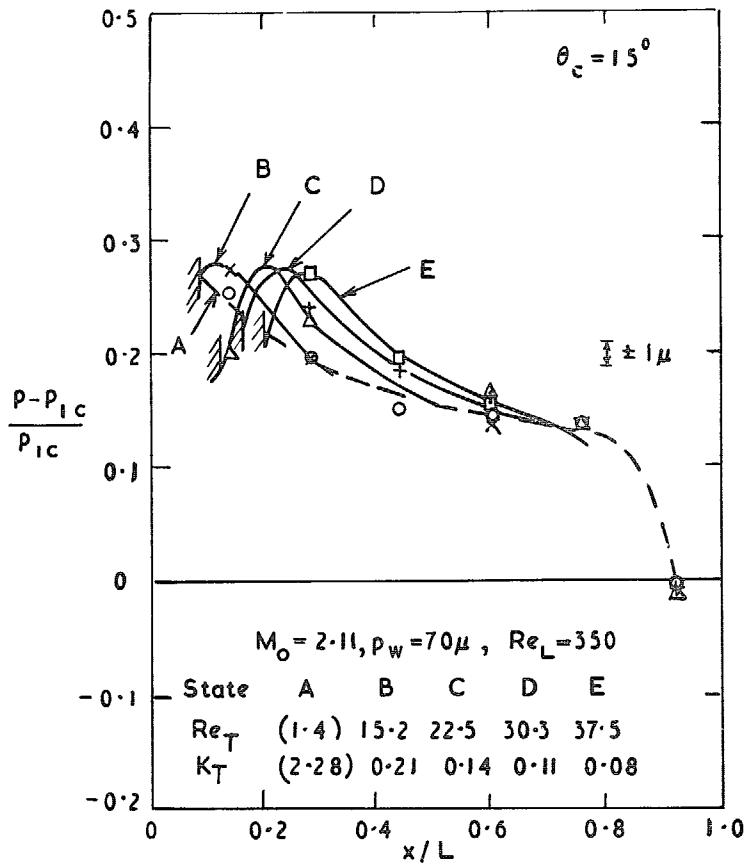FIG. 23a.   Effect of tip truncation on cone-surface pressures.
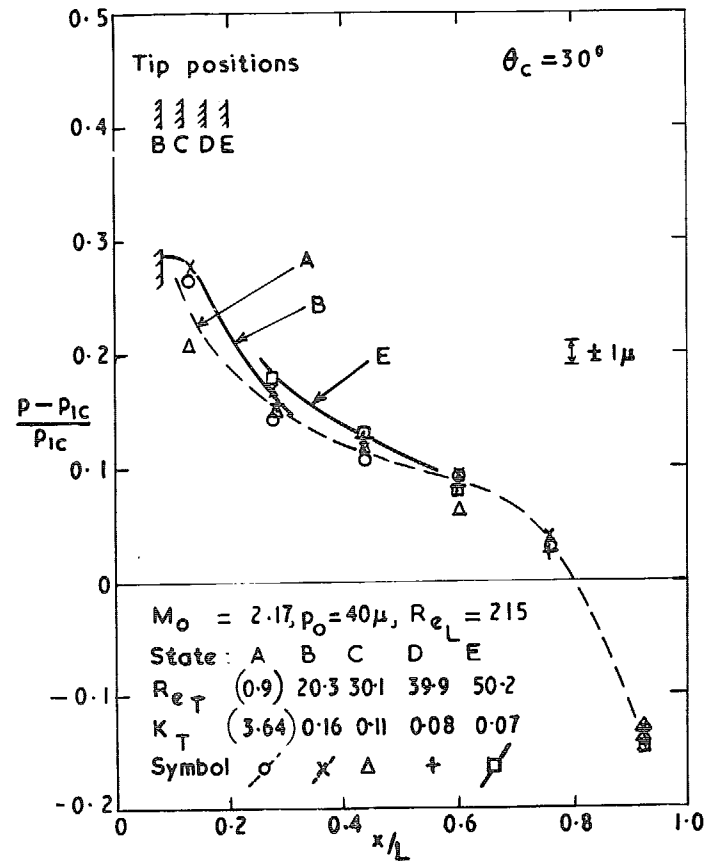
39

FIG. 23b.   Effect of tip truncation on cone-surface
pressures.

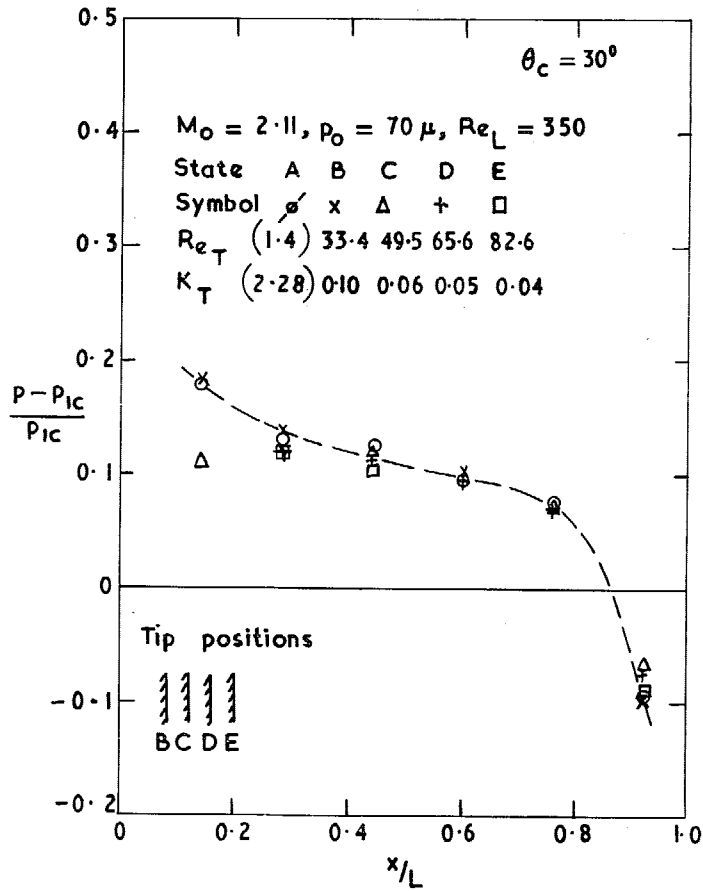FIG. 24a.   Effect of tip truncation on cone-surface
pressures.

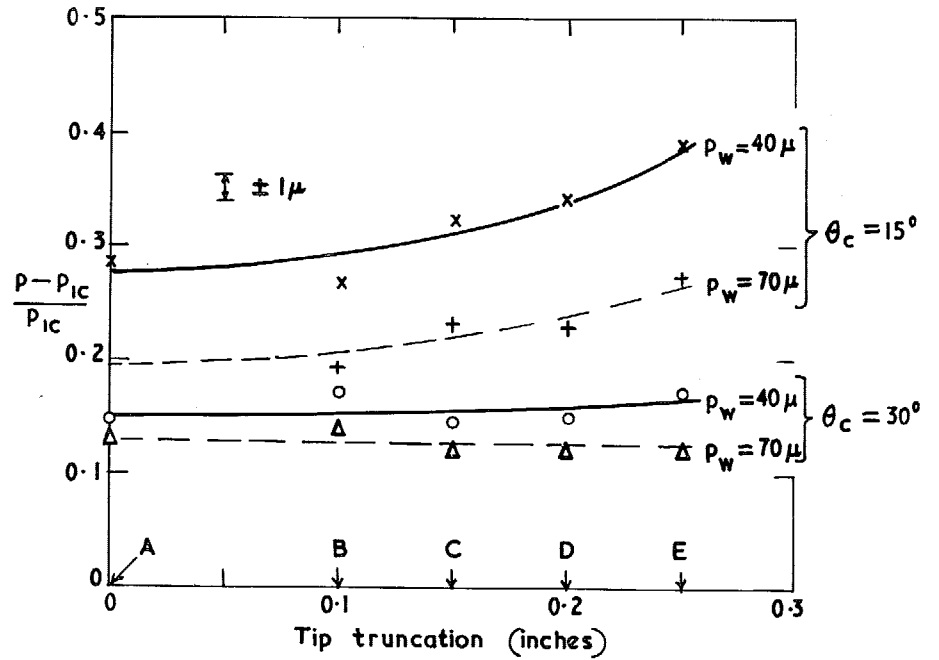FIG. 24b.   Effect of tip truncation on cone-surface
pressures.

FIG. 25.   Influence of cone angle on pressure
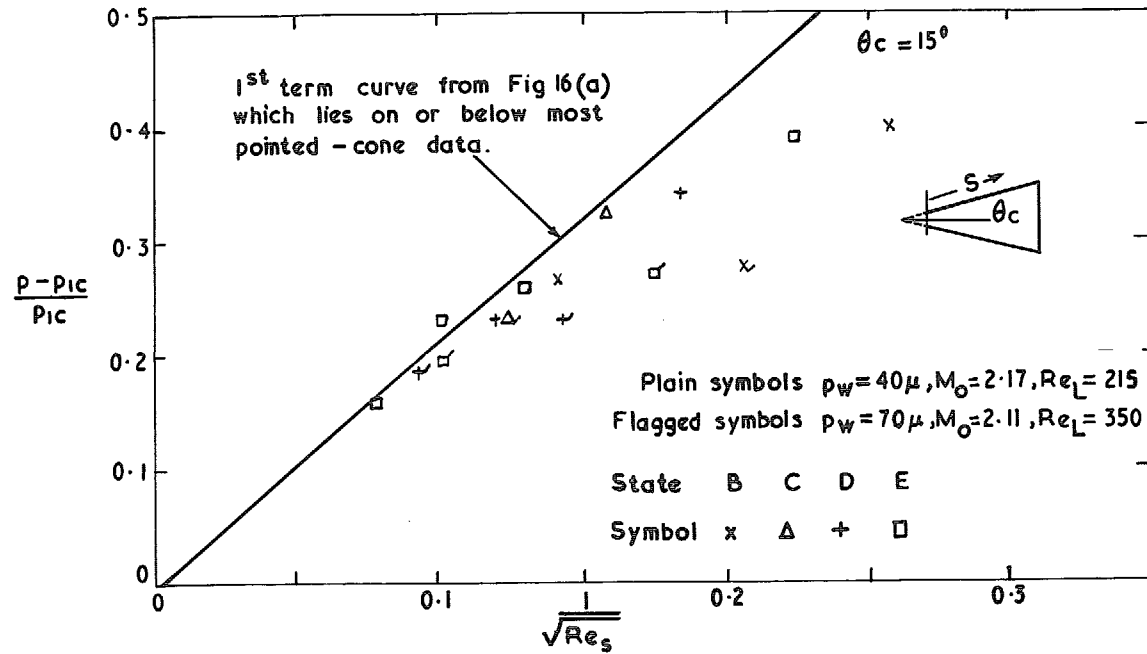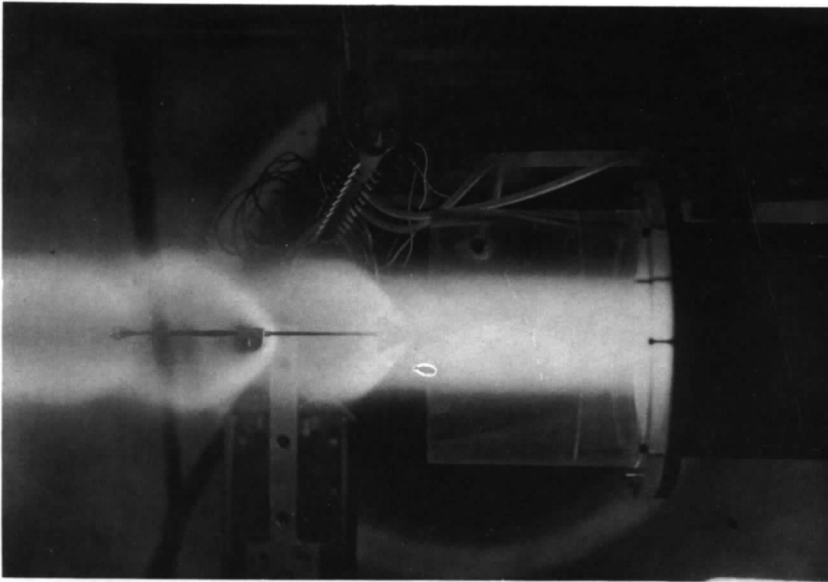changes occuring at hole 2 as the truncation
increases.

$$\frac{P - P_{ic}}{P_{ic}}$$

0·5

0·4

0·3

0·2

0·1

0

$\theta_c = 15^{\theta}$

1st term curve from Fig 16(a)
which lies on or below most
pointed — cone data.

Plain symbols $p_w = 40\mu$, $M_o = 2·17$, $Re_L = 215$

Flagged symbols $p_w = 70\mu$, $M_o = 2·11$, $Re_L = 350$

State   B   C   D   E

Symbol   x   △   +   □

0   0·1 $\dfrac{1}{\sqrt{Re_s}}$ 0·2   0·3
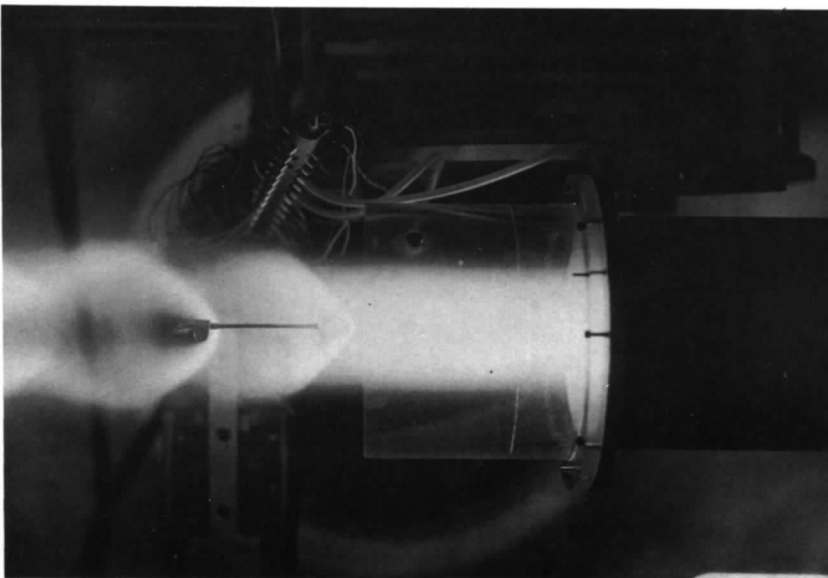
FIG. 26.   Influence of nose bluntness on viscous-induced pressure increment (Holes 1, 2 and 3 only).

State A

State E

FIG. 27. Argon afterglow photographs of flow about sharp and blunt cones with $\theta_c = 30$ deg at a stream pressure of about 25μ (Model withdrawn downstream of skirt exit plane).
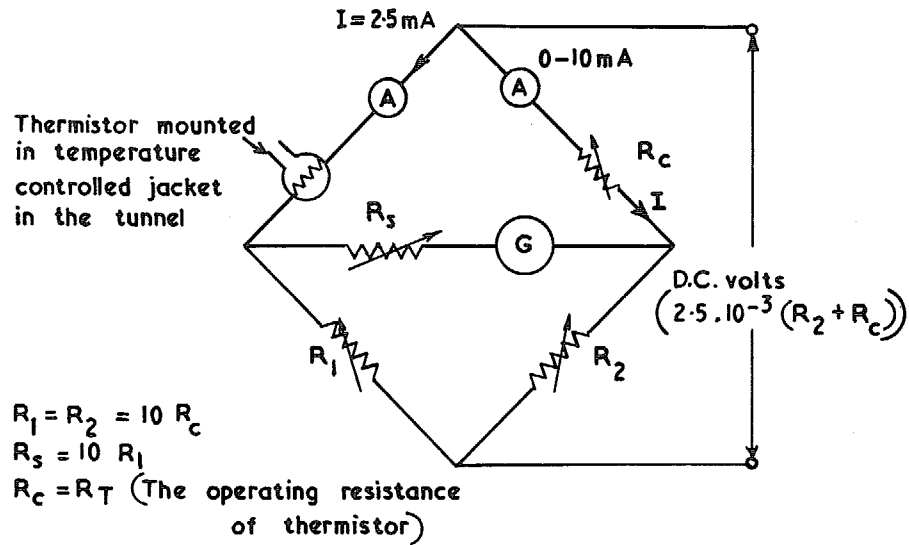
$I = 2.5\,mA$

$0-10\,mA$

Thermistor mounted
in temperature
controlled jacket
in the tunnel

R_c

R_s

I

G

D.C. volts
$\left(2.5 \cdot 10^{-3}(R_2 + R_c)\right)$

R_1

R_2

$R_1 = R_2 = 10\,R_c$
$R_s = 10\,R_1$
$R_c = R_T$ (The operating resistance
of thermistor)

FIG. A1.   Thermistor bridge network for low
pressure measurement.

Calibration for hole No.1.15° cone (1-8-63)
Pressure with McLeod gauge. Free mercury
surface trapped with liquid nitrogen.

Pressure
(μ)

Galvanometer deflection (mm)
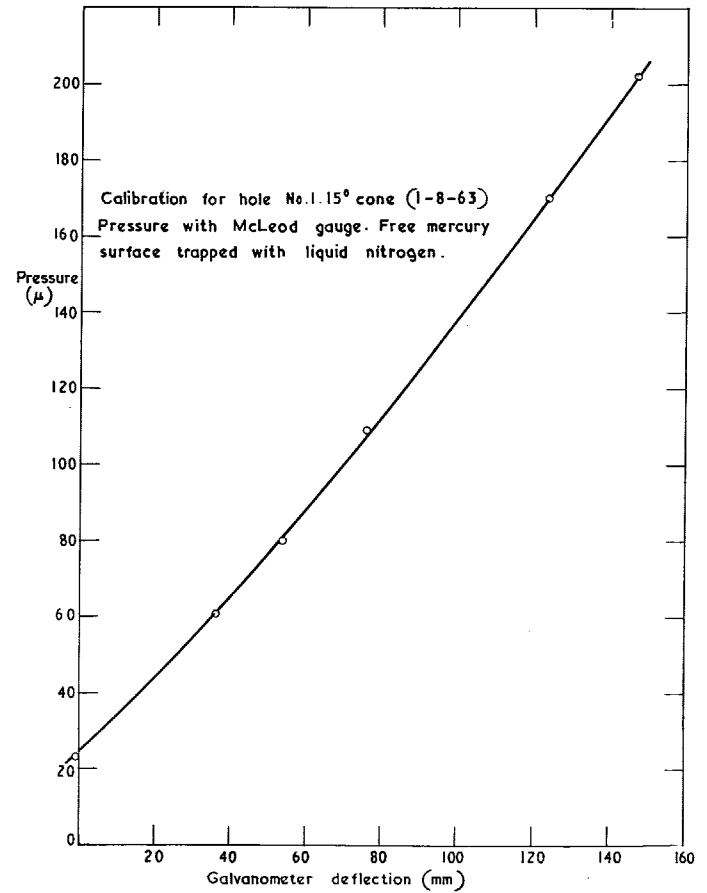
FIG. A2.   Typical   calibration   curve   obtained
during cone tests.